

# A Lattice-Boltzmann CFD study of the hydrodynamics relevant for industrial fermentation processes.

by

**D. Eijsberg**



to obtain the degree of Master of Science  
at Delft University of Technology  
to be defended publicly on Thursday February 2, 2023 at 9:00 AM.

Student number: 4487915  
Project duration: March 14, 2022 – February 2, 2023  
Supervisor: Dr. Ir. C. Haringa  
Thesis Committee: Dr. Ir. C. Haringa  
Dr. Ir. G.B.R. Meesters  
Prof. Dr. S. Kenjereš

---

## Abstract

Fermentation processes are considered to be essential to decrease our reliance on fossil fuel based products. However, the scale-up from lab-scale to industrial-scale has proven to be difficult. Computational Fluid Dynamics (CFD) has the potential to be a tool to optimize the scale-up and to help engineers understand the relevant hydrodynamics inside such reactors. However, traditional CFD simulations are computationally intensive and it is not uncommon that simulations can take several months to compute a few minutes of flow-time. Due to the recent development of GPU-based hardware, the Lattice-Boltzmann method (LBM) has been gaining much interest as this meant an orders-of-magnitude decrease of needed computational time compared to conventional CFD methods. In order to calibrate the models underlying the simulations, the obtained results of said simulations should be validated against experimentally obtained data, which is exceptionally scarce for industrial-scaled reactors.

Hence the aim of this thesis is to investigate the applicability of the LBM in high gas-flow, industrial sized reactors by studying three benchmark cases. Using Large Eddy Simulations (LES) and Euler-Lagrangian tracking of bubble parcels, the models provided by M-Star (M-Star Simulations, LLC) are validated by replicating a small-scale reactor of which the LBM has already been successfully applied to. The industrial-scaled case consists of the simulation of the  $22m^3$  industrial reactor located in Stavanger, which is an exception regarding the scarcity of experimental data for industrial sized reactors. As this data set did not encompass all the relevant data for aerated stirred tanks, the suitability of the LBM and provided models are also tested for a smaller scaled tank of which the Bubble Size Distribution (BSD) throughout the vessel is known. The applicability of the provided models will be tested by comparing the obtained gas hold-up, BSD and power consumption with experimental data sets.

Although the LBM is suitable for industrial-scaled reactors, the provided models by M-Star are not sufficient to predict the gas hold-up and power consumption at high superficial gas velocities. The provided Free Particle drag correlation is not sufficient to describe the dispersion of bubbles throughout the vessel, leading to a significantly under-estimated gas hold-up. In addition, the parcel approach leads to the formation of large bubbles in the vessel. And although enforcing a maximum coalescence diameter does improve the BSD, the gas hold-up is not significantly influenced by the presence of large bubbles. Furthermore, the Euler-Lagrangian way of modeling bubble particles did not lead to the formation of gas cavities, which resulted in an insignificant drop in power consumption. Nevertheless, the current work provides a foundation for subsequent research.

---

# Contents

<b>Contents</b>	<b>ii</b>
<b>List of Figures</b>	<b>vi</b>
<b>List of Tables</b>	<b>viii</b>
<b>1 Introduction</b>	<b>1</b>
1.1 Scope . . . . .	2
1.2 Thesis outline . . . . .	3
<b>2 Theory</b>	<b>4</b>
2.1 Fluid dynamics . . . . .	4
2.1.1 Governing equations . . . . .	4
2.2 Turbulence . . . . .	4
2.3 Bubbles . . . . .	7
2.3.1 Bubble size characterization . . . . .	8
2.4 Hydrodynamic regimes . . . . .	9
2.5 Power consumption Rushton turbine . . . . .	11
<b>3 CFD theory</b>	<b>12</b>
3.1 The Boltzmann transport equation . . . . .	12
3.2 Algorithm: collision and streaming . . . . .	14
3.3 Satisfying the transport equations . . . . .	15
3.4 Turbulence modelling . . . . .	16
3.5 Bubble modelling . . . . .	19
3.5.1 Forces on bubble . . . . .	19
3.5.2 Bubble break-up and coalescence . . . . .	20
3.5.3 Bubble representation . . . . .	20
3.5.4 Fluid-bubble coupling . . . . .	21
<b>4 Computational setup</b>	<b>23</b>
4.1 Computer specifications . . . . .	23
4.2 Geometry . . . . .	23
4.2.1 Case 1: validation case . . . . .	23
4.2.2 Case 2: bubble size distribution . . . . .	24
4.2.3 Case 3: industrial sized Stavanger bioreactor . . . . .	25
4.3 Universal parameters . . . . .	26
4.3.1 Free Ssurface interaction . . . . .	27
<b>5 Results - validation and bubble size distribution</b>	<b>29</b>
5.1 Validation case - lab scale . . . . .	29
5.2 Case 2: lab-scale tank (BSD) . . . . .	30
5.2.1 Gas hold-up . . . . .	30
5.2.2 Bubble size distribution . . . . .	30
5.2.3 Eddy dissipation rate . . . . .	34
5.2.4 Influence of the maximum coalescence diameter parameter . . . . .	34
5.2.5 Contour plots . . . . .	35
5.3 Velocity distribution in the impeller plane . . . . .	37
<b>6 Results - industrial fermentor</b>	<b>39</b>

---

6.1	Gas hold-up . . . . .	39
6.2	Power consumption . . . . .	40
6.3	Comparison CFD techniques . . . . .	43
<b>7</b>	<b>Conclusion and Recommendations</b>	<b>48</b>
7.1	Recommendations . . . . .	48
	<b>Bibliography</b>	<b>50</b>
<b>8</b>	<b>Appendix A</b>	<b>57</b>
<b>9</b>	<b>Appendix B</b>	<b>59</b>
<b>10</b>	<b>Appendix C</b>	<b>61</b>

---

## Abbreviations

Abbreviation	Definition
BSD	Bubble Size Distribution
BGK	Bhatnagar-Gross-Krook
CFD	Computational Fluid Dynamics
CPU	Central Processing Unit
CV	Control Volume
DNS	Direct Numerical Solution
EDR	Eddy Dissipation Rate
GFR	Gas Flow Rate
GPU	Graphics Process Unit
LBM	Lattice-Boltzmann Method
LDA	Laser Doppler Anemometry
LES	Large Eddy Simulation
MRF	Multiple Reference Frame
PIV	Particle Image Velocimetry
RANS	Reynolds-averaged Navier Stokes
RPM	Rotations Per Minute

## Symbols

Symbol	Definition	Unit
$c_i$	Discrete Velocity	[-]
$d_{10}$	Arithmic Mean Diameter	[m]
$d_{32}$	Sauter Mean Diameter	[m]
$d_{43}$	De Broucke Mean Diameter	[m]
$d_e$	Maximum stable Bubble Size	[m]
$f$	Particle Distribution Function	$[kg\ s^3/m^6]$
$f_i$	Discrete-Velocity Distribution Function	$[kg\ s^3/m^6]$
$g$	gravity	$[m/s^2]$
$p$	Pressure	[Pa]
$u$	Fluid Velocity	[m/s]
$u_c$	Characteristic Velocity	[m/s]
$\mathbf{v}$	Flow velocity vector	[m/s]
$w_i$	Weighting Coefficient	[-]
$C_s$	Smagorinsky Coefficient	[-]
$D$	Impeller Diameter	[m]
$N$	Rotational Speed	[1/s]
$N_p$	Power Number	[-]
$P_o$	Power Input	[W]
$Q_g$	Gas flow rate	$[m^3/s]$
$Re$	Reynolds Number	[-]
$Re_a$	Reynolds Approach Number	[-]
$S_{ij}$	Strain Rate Tensor	[-]
$T$	Tank Diameter	[m]
$U_a$	Approach Velocity	[m/s]
$\epsilon$	Eddy Dissipation Rate	[W/kg]
$\zeta$	Microscopic Velocity	[m/s]
$\eta$	Kolmogorov Microscale	[m]
$\kappa$	Eddy Wavenumber	[1/m]
$\lambda$	Taylor Microscale	[m]
$\mu$	Viscosity	[kg/m.s]
$\nu$	Kinematic Viscosity	$[m^2/s]$
$\rho$	Density	$[kg/m^3]$
$\sigma$	Surface Tension	[N/m]
$\tau$	Torque	[N/m]
$\phi$	Gas Hold-up	[%]
$\omega$	Angular Velocity	[1/s]
$\Omega$	Collision Operator	[-]
$\ell$	Integral Eddy Size	[m]

---

## List of Figures

1	Design parameters. . . . .	1
2	Turbulent energy cascade . . . . .	5
3	Energy spectrum of the turbulent eddies. . . . .	6
4	Representation of the different hydrodynamics regimes. . . . .	10
5	Transition between hydrodynamic regimes for the 22m <sup>3</sup> bioreactor. . . . .	11
6	Graphical display of the three scales. . . . .	12
7	Visual representation of the D3Q19 velocity set. . . . .	13
8	Graphical representation of the collision and streaming step on a D2Q9 lattice. . . . .	15
9	The turbulent fluid velocity can be decomposed in a time-averaged and fluctuating component. . . . .	17
10	Comparison of DNS, LES and RANS turbulence modelling. . . . .	17
11	Visual display of the turbulent wavelengths which are not simulated when a LES filter is used. . . . .	18
12	The vessel of the validation case. . . . .	24
13	Representation of the cross-section of the tank in between two baffles. . . . .	24
14	Geometry of the Stavanger case . . . . .	26
15	Bubble accumulation at the free surface. . . . .	28
16	Bubble count for the validation case. . . . .	29
17	Comparison of the obtained bubble size distribution at a gas flow rate of 0.0164 m <sup>3</sup> /s. . . . .	31
18	Comparison of the obtained bubble size distribution at a gas flow rate of 0.0438 m <sup>3</sup> /s. . . . .	32
19	Comparison of the obtained bubble size distribution at a gas flow rate of 0.0687 m <sup>3</sup> /s. . . . .	33
20	Non-dimensional Eddy Dissipation Rate . . . . .	34
21	Comparison of the influence of the specified max coalescence diameter for an agitation rate of 180 RPM. . . . .	35
22	Contour plot of the gas fraction, 180 rpm; 0.00164 m <sup>3</sup> /s. . . . .	36
23	Contour plot of the gas fraction at an agitation speed of 385 rpm and GFR of 0.00687 m <sup>3</sup> /s. . . . .	36
24	Contour plot of the fluid velocity at the impeller plane for an agitation rate of 385 rpm and a GFR of 0.00687 m <sup>3</sup> /s. . . . .	38
25	Gas hold-up as a function of RPM and GFR. . . . .	39
26	Normalized EDR. . . . .	41
27	Velocity and bubble volume fraction contour plot at the impeller plane. . . . .	42
28	Fluid volume fraction contour plot . . . . .	43
29	Power number of the impeller as a function of time. . . . .	44
30	Comparison of the gas hold-up between the LB-CFD and FV-CFD approach. . . . .	45
31	Hisogram for a maximum coalescence diameter of 5mm. . . . .	46
32	Hisogram for a maximum coalescence diameter of 2.5cm. . . . .	47
33	EDR per output line for the case with an agitation speed of 180 RPM and GFR of 0.00164 m <sup>3</sup> /s. . . . .	57
34	EDR per output line for the case with an agitation speed of 385 RPM and GFR of 0.00687 m <sup>3</sup> /s. . . . .	58
35	Bubble Settings . . . . .	59
36	Wall Settings . . . . .	60
37	Free Surface Settings . . . . .	60
38	Grid convergence for the verification case. As dx is increased, the Power number converges. . . . .	61

---

39	Bubble fluctuations with extended run time. . . . .	61
----	---	----

---

## List of Tables

3	Geometry of the considered cases . . . . .	23
4	Specifications of the twelve different cases . . . . .	25
5	Injection scales used for the parcel approach for the different gas flow rates. . . . .	26
6	Comparison between discrete and parcel bubble representation. . . . .	29
7	Gas hold-up comparison for the experimental obtained values and the LB CFD results . . . . .	30
8	Comparison of the LBM and experimental values for the gas hold-up. . . . .	39
9	CFD results for the ungasged power consumption. . . . .	40
10	Estimated power consumption of the experiment. . . . .	41
11	$P_g/P$ for different aeration rates and agitation speeds. . . . .	41
12	Comparison of the obtained results for LB-CFD, FV-CFD and experimental results	43

# 1 Introduction

Fermentation processes have been widely used throughout history and are nowadays considered to be an important technology which will help us to decrease our reliance on fossil fuel based products[1]. In order to become cost-competitive in the fossil-dominated bulk-markets, optimization of fermentation processes is of utmost importance to enhance the biological performance of the microbes involved in fermentation[2].

The key performance indicators of bioprocesses are titer, rate and yield[3][4]. These indicators are dependent on a lot of physical phenomenon present in bioreactors. Figure 1 depicts different parameters which can be optimized in order to increase the yield of the product. These parameters include -but are not limited to- operating conditions, kinetics, and oxygen transfer rate. Despite there being exceptions (such as bioethanol from glucose), many bioprocesses are dependent on interphase mass transfer and are thus aerated[5][6]. Most often these processes are supplied with oxygen functioning as an electron acceptor to make the process become thermodynamically feasible[7][8]. Oxygen transfer to the liquid phase is often the rate limiting step for productivity, and is therefore considered to be an essential step in order to improve the productivity of the microbial processes[9]. In addition to such aerobic conditions, there has been much attention for fermentation processes using gaseous substrates such as carbon dioxide, carbon monoxide, hydrogen and methane which requires interphase mass transfer from the substrate to the fluid as well [10][11].

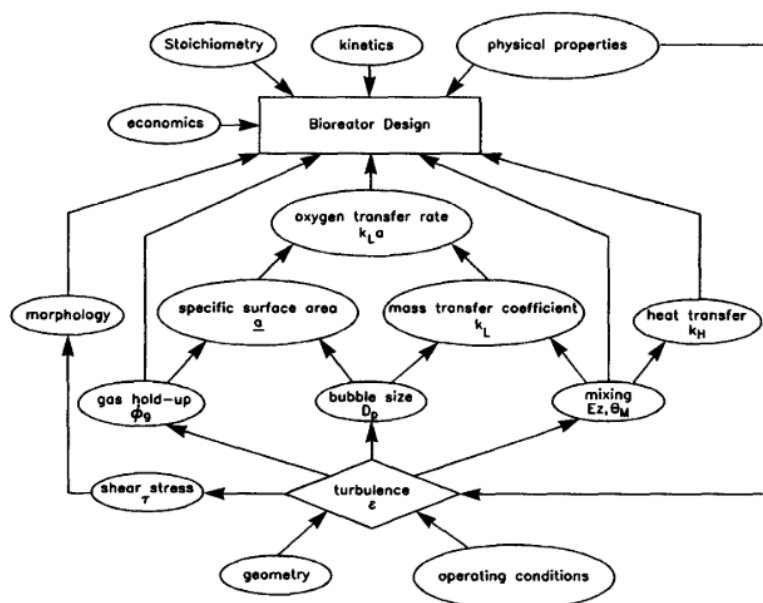


Figure 1: Design parameters which are considered to improve the yield of the bioreactor[12].

The scale-up of (bio)reactors from lab-scale to industrial scale is a major goal for scientist and engineers [13]. This has proven to be difficult as the hydrodynamics in reactors tend to change when the volume of the reactor is increased, which results in a lower mass transfer rate [14]. Rational optimization of industrial bioreactors requires knowledge about the gas hold-up and bubble size distribution throughout the vessel, which are a direct manifestation of bubble break-up and coalescence. It is however a great challenge to obtain experimental data about the local bubble size distribution inside of (industrial-scale) reactors [15][16][17]. Computational Fluid Dynamics (CFD) can be a tool in order to optimize the scale-up of bioreactors and to let engineers predict the transfer of oxygen to liquid at conditions applicable on an industrial scale, at which it is hard to gather experimental data [18][19]. CFD simulations are however

---

computationally intensive and it is not uncommon for traditional CFD simulations of multi-phase reactors, typically conducted on CPUs, to take several months of runtime to simulate a few minutes of flow-time [20].

The last few years saw a significant development of GPU-based hardware which, in contrast to CPUs, contain thousands of cores which are developed to be able to execute tasks in parallel which speeds up said simulations with orders-of-magnitude. Thus, algorithms were developed in order to exploit the benefits of GPU's and recently, the Lattice Boltzmann Method (LBM) has been gaining much interest since its inception in 1988[21]. This is due to its wide range of applicability in various engineering areas and the numerical structure of the LBM which makes it highly suitable for computational parallelization, enabling the method to fully exploit the GPU architecture [22][23]. This led to the establishment of GPU-driven LBM CFD which transcends conventional CFD approaches by orders-of-magnitude[22][23]. Because of this performance increase, many physics and model simplifications can be revoked and first-principle transport physics can be called upon, such as transient modelling of the fluid flow instead of a time-averaged flow field [21].

The results obtained with CFD simulations should be validated with experimental data in order to calibrate the models underlying the simulations, which is especially scarce for industrial-scale reactors with high gas flow rates[6]. An exception to the scarcity of experimental data on this scale to this is a set of experimental data available from an industrial sized 30  $m^3$  bioreactor in Stavanger located in Norway [6]. This data encompasses the power consumption, gas hold-up, mixing time, liquid velocities [24] and biokinetic data [25]. Furthermore, this particular case has already been simulated with conventional CFD tools using a  $k-\epsilon$  turbulence model and the multiple reference frame (MRF) model[26].

## 1.1 Scope

Although the LBM has been successfully implemented to study topics ranging from i.e. heat transfer, chemical reactions and multi-phase reactors, there have been relatively few studies considering aerated tanks for industrial applications[27][28]. One of the exceptions is the study of a 160  $m^3$  by Bernauer et al.[29]. In this study, bubbles were modeled using the Euler-Lagrangian approach, implicating that bubbles are modeled as spherical point particles with negligible volume. As such, the bubbles had no influence on the fluid level in the simulations[30].

Hence the aim of this thesis is to investigate the applicability of the LBM in high gas-flow, industrial sized reactors by studying three benchmark cases. The large-scale case explores the simulation of the Stavanger industrial reactor. Since the experimental data from Stavanger does not cover all relevant data of agitated stirred tanks, like the bubble size distribution throughout the vessel, the suitability of the LBM is also tested for a smaller lab scale reactor for which such data is available[31]. These simulations are validated by testing the performance of the LBM of a small reactor of which the LBM has already been applied to[32]. The simulations are performed using M-Star CFD (M-Star Simulations, LLC) with the Large Eddy Simulations (LES) turbulence model and Euler-Lagrangian tracking of bubbles which continuously experience break-up and coalescence events. In addition, the considered bubbles do have an effect on the liquid level throughout the simulations. Besides testing the applicability of the LBM, the influence of the physical models provided by M-star is investigated and guidelines are provided for subsequent research.

---

The research objectives hence are:

- Replicate the small-scale reactor simulation by Thomas [32] to use as a validation for the chosen parameters
- Set up the mid-sized reactor and determine the bubble size distribution and gas hold-up predicted by the simulations and compare the results with experimental data[31].
- Simulate the industrial-scale reactor of Stavanger and compare the obtained results of gas hold-up and power consumption with experimental data and previously conducted CFD research[24][25][26].

The main research question is thus:

- Can the LBM-CFD using Large Eddy Simulations predict the bubble size distribution, gas hold-up and power consumption at different agitation rates, high superficial gas velocities and vessel volumes?

## 1.2 Thesis outline

This thesis is comprised of seven chapters, starting with the introduction. The second and third chapter cover respectively the physical and LBM theory underlying the simulations. The computational set-up will be discussed in the fourth chapter. The results of the small-scaled reactors will be discussed in the fifth chapter, while the sixth chapter provides the results of the industrial scale fermentor. Finally, the conclusion will be presented in the seventh chapter together with a set of recommendations for further research.

---

## 2 Theory

The aim of this chapter is to introduce the physical theory which underlies the models used in the Lattice-Boltzmann method in order to simulate the reactors. At first an overview is given of the essential transport equations governing fluid flow, whereafter the phenomenon called turbulence is covered. As this thesis focuses on multiphase reactors, bubble behaviour such as break-up, coalescence and hydrodynamic regimes present in the vessels are discussed.

### 2.1 Fluid dynamics

In order to be able to understand and describe what the flow in the fermentor will be, the physics underlying fluid flow must be understood.

#### 2.1.1 Governing equations

Equation 2.1 and Equation 2.2 are respectively the continuity and the Navier-Stokes equations, and are the fundamental equations describing the flow of fluids and gases. In these equations  $\rho$  is the density [ $\text{kg}/\text{m}^3$ ],  $\mathbf{v}$  is the flow velocity vector field [ $\text{m}/\text{s}$ ],  $t$  is the time [ $\text{s}$ ],  $p$  is the pressure [ $\text{Pa}$ ],  $\mu$  is viscosity [ $\frac{\text{kg}}{\text{m}\cdot\text{s}}$ ] and  $g$  is the gravity [ $\text{m}/\text{s}^2$ ]. The continuity equation describes the conservation of mass, while the Navier-Stokes equation describes the conservation of momentum. Together they form a set of equation which are sufficient to describe the flow of fluids. However, because of the non-linearity of the Navier-Stokes equation, it is not (yet) analytically solvable except for a few cases. During this research, only turbulent flow is considered and therefore laminar flow will only be briefly touched upon.

$$\frac{\partial \rho}{\partial t} + \rho \nabla \cdot \mathbf{v} = 0 \quad (2.1)$$

$$\frac{\partial \rho \mathbf{v}}{\partial t} + \rho (\mathbf{v} \cdot \nabla) \mathbf{v} = -\nabla p + \mu \nabla^2 \mathbf{v} + \rho \mathbf{g} \quad (2.2)$$

### 2.2 Turbulence

Fluid flow will be laminar if the viscosity of the fluid is able to suppress the inertial forces. This is characterized by fluid particles following a smooth trajectory. However when the velocity is increased (or the viscosity lowered), the non-linearity of the Navier-Stokes equation will lead to unpredictable chaotic motion, with even infinitesimal changes to initial conditions leading to changes in the consequent motion and the fluid flow will be turbulent. This happens when the viscosity is unable to suppress the instabilities inherent to fluids created by the inertial forces. These instabilities create eddies, which will break up into smaller eddies. As the eddies break up they will pass on their inertial energy onto the smaller eddies, until the viscosity can suppress the inertial forces driving the breakup[33]. This cascade of energy is depicted in Figure 2.

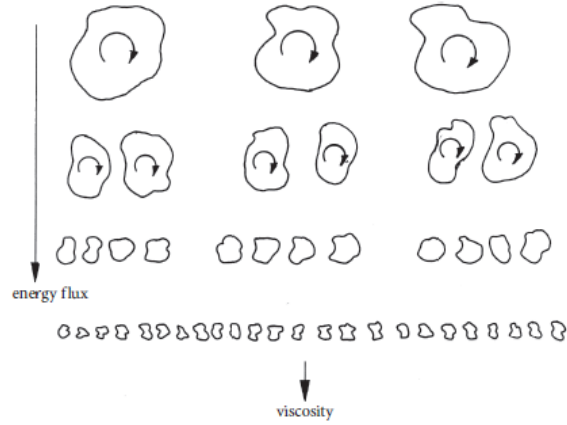


Figure 2: The energy cascade in turbulence. The largest eddies break up and pass on their kinetic energy onto the smaller eddies until the viscosity is able to overcome the inertial forces[33].

The largest eddies in the vessel have a size which is order-of-magnitude consistent with the tank diameter[34]. These large eddies are called integral eddies, are depicted by  $\ell$ , and are anisotropic in nature. Kolmogorov’s theory of isotropic turbulence states that, when an eddy is small enough, the fluctuating components of the velocity can be considered equal, and thus can be considered as isotropic[35]. Although turbulence itself is not isotropic, the assumption of local isotropic turbulence may be very useful at small length scales like the bubble diameter, which will be explained upon later[9][12].

The Taylor microscale is depicted as  $\lambda$  and represents the scale at which the large anisotropic eddies transition into localized isotropic eddies[32][36]. The length scale at which this transition takes place is described by Equation 2.3[37]:

$$\frac{\lambda}{\ell} = \frac{\lambda}{T} \approx \sqrt{\frac{15}{Re}} \quad (2.3)$$

in which T is the tank diameter[m] and Re is the impeller Reynolds number, which is described by Equation 2.4. In this equation N represents the rotational speed [1/s], D the impeller diameter [m] and  $\nu$  is the kinematic viscosity of the fluid [ $m^2/s$ ]:

$$Re = \frac{ND^2}{\nu} \quad (2.4)$$

The cascade of eddy decay continues until the eddy size is so small that viscous forces overcome the inertial forces. The kolmogorov length scales represents these eddies which are the smallest hydrodynamic length scales in the reactor and is represented as  $\eta$ . The size of these eddies are directly related to the Reynolds number, and is shown in Equation 2.5, in which T is the diameter of the vessel[33].

$$\eta_k \approx \frac{\ell}{Re^{3/4}} \approx \frac{T}{Re^{3/4}} \quad (2.5)$$

As can be seen from Equation 2.3 and Equation 2.5, the Taylor and Kolmogorov length scales are directly related to the (impeller) Reynolds number and will decrease in size when the Reynolds number is increased. Within these length scales the largest eddies contribute to bulk mixing of the fluid while the small Taylor length eddies contribute to micromixing phenomena <sup>1</sup>.

<sup>1</sup>”Predicting Mass Transfer (KLA) in Gasified Bioreactors.” M-Star Simulations, LLC, docs.mstar CFD.com/tutorials/kLA.html. Accessed 19 Sept. 2022.

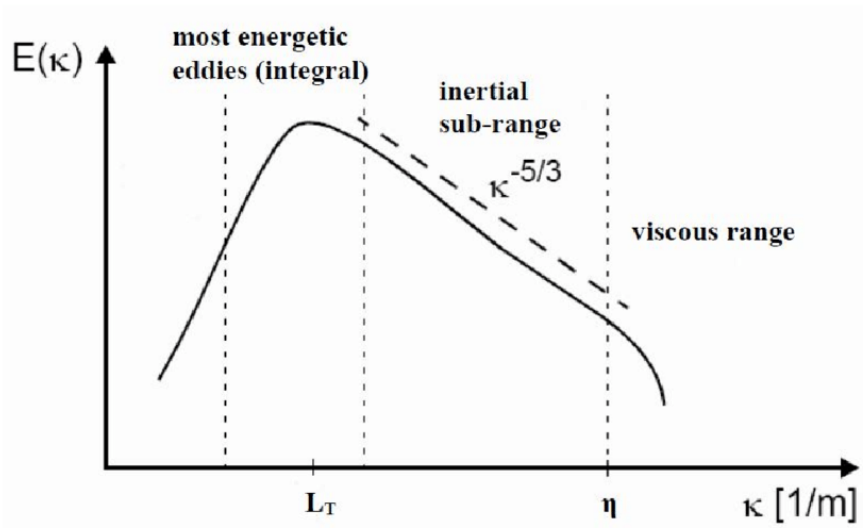


Figure 3: Energy spectrum of the turbulent eddies[38].

Within fully developed turbulence a broad range of eddy sizes exist. For depicting the energy of those eddies it is common to utilize the wavenumber of the eddy instead of the eddy size[33]. The wavenumber is represented by  $\kappa$  and is inversely correlated to the eddy size, meaning that a higher wavenumber corresponds with a smaller eddy size. Figure 3 shows the energy spectrum of the turbulent eddies. It can be seen that energy is generated by the largest eddies present in the system. The intermediate sized eddies contain the bulk of the kinetic energy, and are also named the “energy containing eddies”. In the inertial subrange, the kinetic energy is transferred unto smaller eddies and is dependent to the wave length as  $\kappa^{-5/3}$ . The smallest eddies do not contribute significantly to the total energy, but they are continuously energized by the larger eddies while they dissipate their energy in the fluid[12]. The energy dissipation rate is calculated from:

$$\epsilon \sim \nu S_{ij} S_{ij} \quad (2.6)$$

where  $\epsilon$  is the energy dissipation rate (EDR) and has the units of [W/kg],  $\nu$  is the kinematic viscosity of the fluid, and  $S_{ij}$  is the strain rate tensor. The strain rate tensor is given by Equation 2.7.

$$S_{ij} = \frac{1}{2} \left( \frac{\partial u_i}{\partial x_j} + \frac{\partial u_j}{\partial x_i} \right) \quad (2.7)$$

It can be seen that the energy dissipation rate is thus dependent on gradients in velocity, and is the largest in area’s where these gradients are the largest. Using Kolmogorov’s theory of isotropic turbulence, the order of magnitude of the energy dissipation rate can be estimated from Equation 2.8, where  $u_c$  is the characteristic velocity of the vessel[12]. The order of magnitude of the eddy dissipation rate can thus be estimated from the velocity agitated by the turbine, and the length scale of the vessel. The magnitude of the eddy dissipation rate can vary significantly throughout the vessel, with the difference between local and average EDR being over three orders of magnitude[39].

$$\epsilon \sim \frac{u_c^3}{\ell} \quad (2.8)$$

---


$$\eta \sim \ell \text{Re}^{-3/4} \text{ or } \eta = (\nu/\epsilon)^{1/4} \quad (2.9)$$

The eddy dissipation rate  $\epsilon$  can be made dimensionless ( $\bar{\epsilon}$ ) by Equation 2.10. This can prove useful in order to compare eddy dissipation rates at the impeller computed with CFD simulations with experimental data.

$$\bar{\epsilon} = \frac{\epsilon}{N^3 D^2} \quad (2.10)$$

### 2.3 Bubbles

In agitated air-sparged reactors, the bubble size plays a crucial role[40]. Small bubbles are usually preferred as a larger interfacial area leads to an increase of mass transfer to the liquid phase[40]. However, bubbles occur in a tank with a certain bubble size distribution which is characterized in the form of a histogram[41]. Knowledge about the bubble size distribution is vital in order to determine the overall mass transfer to the liquid. Unfortunately it is of great difficulty to obtain experimental data about the local bubble size in a reactor[31]. In addition to a small bubble size, a higher gas hold-up is desired in order to maximize mass transfer.

Although the hydrodynamics in a multiphase reactor are very complex, Kolmogorov's theory of isotropic turbulence has been successfully utilized to describe the relevant hydrodynamic phenomena. Despite this theory being a simplified version of reality, it will lead to models which are much simpler to adopt, and thus provides an attractive basis for rational design of bioreactors[12].

Within a multiphase agitated tank, there are typically three variables which have a direct influence on bubble break-up and coalescence rates and thus the bubble size: the impeller speed, airflow rate and surfactants which might be present[40].

Bubble break-up is caused by the turbulent eddies generated by the rotating impeller. A bubble will break when the energy dissipation rate of the fluid exceeds the surface energy of the bubble[21]. Based on Kolmogorov's theory of isotropic turbulence, the maximum bubble size which is stable against break-up is estimated to be[42]:

$$d_e = C_1 \frac{\sigma^{3/5}}{\rho^{3/5} \epsilon^{2/5}} \quad (2.11)$$

where the constant  $C_1$  is determined to be 0.7[12]. From Equation 2.11 it can be seen that the maximum stable bubble size is dependent on the surface tension, the density of the fluid and the eddy dissipation rate created by the impeller. It is recognized that the maximum stable bubble size will decrease when the eddy dissipation rate is increased[32]. However, it must be stated that Equation 2.11 is based on a dimensional analysis based on first principles turbulence theory, and therefore is an estimation of the maximum stable bubble size for the specified EDR. As the EDR varies significantly throughout the vessel, the maximum stable bubble size will also fluctuate due to the EDR[12].

Although eddies must have enough energy in order to break the bubble, very large eddies will not cause break-up as they are so large that they will only cause movement of the bubble[15].

Besides bubble break-up, bubbles can also undergo coalescence when bubbles interact with each other. Bubble coalescence is a complex mechanism which occurs as a three-step process. These steps can be summarized as follows. Bubbles will approach each others within a range of 10-100  $\mu m$ , and a small liquid layer will be confined between the bubbles. Next, the liquid layer

---

between the bubbles is drained and will thin to 0.01-0.1  $\mu m$ . At the last stage, the liquid film layer will rupture resulting in bubble coalescence. The second and last stage are considered to be the rate-limiting steps in the bubble coalescence process[12][15][21].

Bubble coalescence is inherently correlated to bubble collisions. Bubble collision mechanism can be differentiated into collisions rising from turbulence, buoyancy and laminar shear. These three mechanisms are assumed to be cumulative, but for the present cases turbulent collisions are assumed to be dominant[9].

Eddies within the integral length scale are predominantly responsible for the transport of large quantities of bubbles while not contributing significantly to the relative motion between neighbouring bubbles. Meanwhile very small eddies do not carry enough energy to have a significant impact on the motion of bubbles. Therefore it is customary to assume that eddies within the inertial scale which are of the same length scale as the bubble size are primarily responsible for the relative motion between bubbles and are therefore responsible for bubble collisions[9][12]. This assumption is shown in Equation 2.12.

$$\kappa_\ell \ll d_b \ll \kappa_\eta \quad (2.12)$$

As stated, the rate limiting step in bubble coalescence is that bubbles will need to stay in contact long enough in order to remove the liquid film layer between the bubbles such that it can rupture. Because of this temporal restriction, turbulent eddies within the inertial scale can also separate the bubbles while they are in contact with each other. Therefore, a lot of collisions will not result in bubble coalescence, especially in areas with a high local turbulent kinetic energy[15][43].

The approach Reynolds number,  $Re_a$  is dimensionless number which can predict whether two bubbles will coalesce. The equation for this number is shown in Equation 2.13, where  $U_a$  is the approach velocity of the two bubbles,  $d_h$  is the harmonic mean bubble diameter of the bubble pair and  $\sigma$  is the surface tension.

$$Re_a = \frac{U_a d_h}{\sigma} \quad (2.13)$$

It is experimentally deduced that, for bubble coalescence to take place, the approach Reynolds number should be not exceed 40[44]. When the approach Reynolds number exceeds 40, bubbles will not coalesce but experience an elastic bounce. What this indicates is that the approach velocity of two bubbles should not be too high, but also that the mean bubble size should not be too large. Larger bubbles have a large collision frequency, but they also require a longer contact time in order to coalesce and thus the probability of eddies separating the bubble pair is bigger[9].

### 2.3.1 Bubble size characterization

In a bioreactor, millions of bubbles can be simultaneously present in the system. As these bubbles come in different sizes, it is hard to obtain the total interfacial area of all bubbles combined in order to determine the mass transfer rate. There are multiple ways to characterize the mean bubble diameter. The Sauter mean diameter is one way to express the average size of all the bubbles present in the system[41][45]:

$$d_{32} = \frac{\sum_1^N n_i d_i^3}{\sum_1^N n_i d_i^2} \quad (2.14)$$

---

The Sauter mean diameter,  $d_{32}$  is also called the volume-to-surface area (or the mean surface diameter)[31]. It is a practical criterion as it provides a way to relate the total interfacial area with the gas hold-up, shown in Equation 2.15[31]:

$$a = \frac{6\varepsilon}{d_{32}} \quad (2.15)$$

Equation 2.15 shows the formula to calculate the total interfacial area and highlights the relation between the  $d_{32}$  and the gas hold-up[31]. Another way to characterize the bubble sizes is by using the  $d_{10}$  criterion which, unlike the  $d_{32}$ , is the mean average of all bubbles present in the system:

$$d_{10} = \frac{\sum d_i}{n} \quad (2.16)$$

The De Brouckere mean diameter  $d_{43}$ , also called the volume-weighted mean diameter, characterizes the mean diameter by averaging the particles over volume as, and is thus more susceptible to bubbles with a larger volume[46].

$$d_{43} = \frac{\sum_1^N n_1 d_i^4}{\sum_1^N n_1 d_i^3} \quad (2.17)$$

When comparing the values of  $d_{10}$  with  $d_{32}$ , it was found that  $d_{10} < d_{32} < d_{43}$  as  $d_{10}$  is more susceptible to the smallest bubbles present in the system[47].

## 2.4 Hydrodynamic regimes

When looking at an air-sparged agitated tank, it is important to differentiate between the different bulk flow regimes of the bubbles within the tank as the different regimes have an impact on the total gas hold-up, scale-up and design of the reactors[48]. Figure 4 shows a schematic picture of the different bulk flow patterns of the bubbles within an agitated tank. There are typically three regimes which can be differentiated from each other. The first regime is the flooded regime where the gas flows through the impeller plane up to the surface of the liquid. This happens when the impeller does not provide sufficient force to disperse the bubbles throughout the vessel. When impellers rotate, trailing vortices are generated in the flow field behind the impeller blades[49]. When the impeller speed is increased, gas cavities form inside those vortices[50]. The impeller creates enough turbulence in order to disperse the bubbles above the impeller plane, but not strong enough to create circulation of the bubbles below the impeller. Complete dispersion, or circulation, is caused when the impeller creates sufficiently strong turbulence such that the bubbles are circulated below the impeller plane. Whether impeller flooding or dispersion is achieved thus balances on a trade-off between impeller power and the gas flow rate. A higher gas flow rate will require a higher impeller power in order for the bubbles to be dispersed.

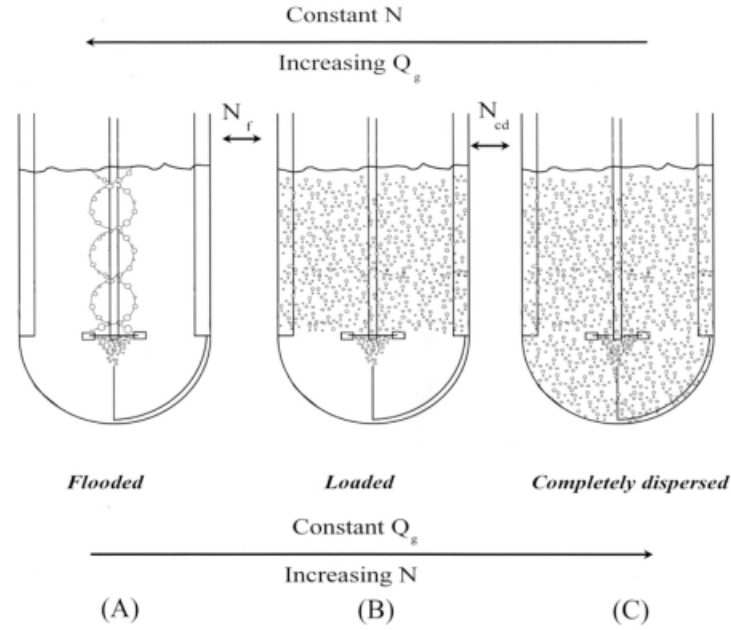


Figure 4: Representation of the different hydrodynamic regimes: (A) flooded, (B) Loaded, (C) Completely Dispersed[48].

The transition from the flooding to the dispersion regime can be described by a linear relationship between the dimensionless Froude number ( $Fr$ ) and the dimensionless gas flow number ( $Fl_g$ )[51]. The Froude number is the ratio of turbine induced inertia with gravity and is shown in Equation 2.18. The gas flow number is shown in Equation 2.19, where  $Q_g$  denotes the superficial gas flow rate [ $m^3/s$ ].

$$Fr = \frac{N^2 D}{g} \quad (2.18)$$

$$Fl_g = \frac{Q_g}{ND^3} \quad (2.19)$$

For the 30  $m^3$  bioreactor, a fluid flow map has been designed which depicts the transitions between the regimes as a function of the Froude and Gas Flow Number. This flow map is shown in Figure 5.

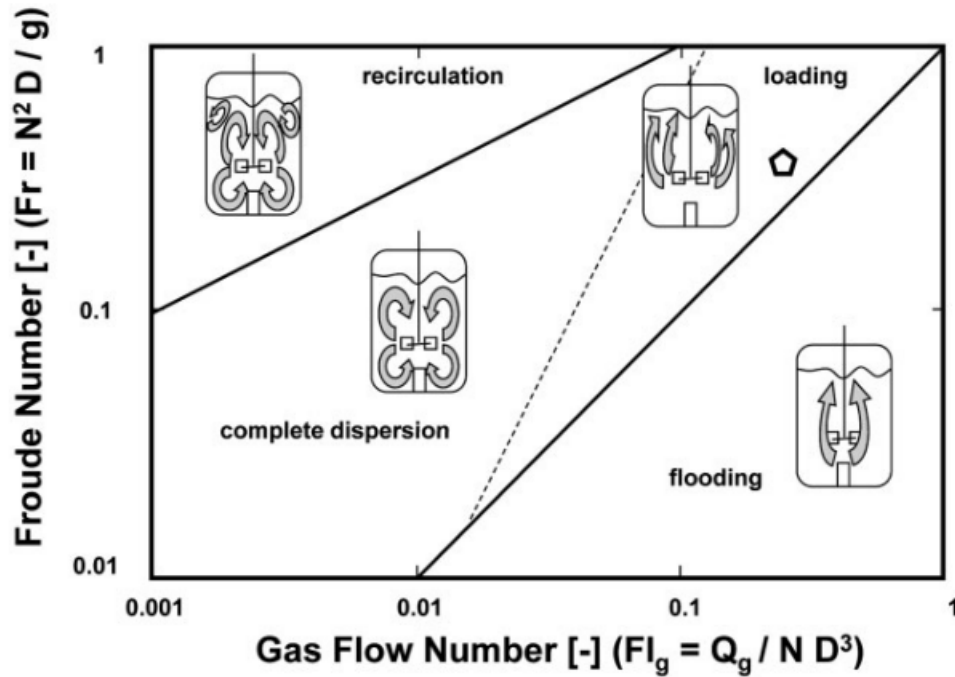


Figure 5: Representation of the transition between hydrodynamic regimes for the  $22m^3$  bioreactor[6].

## 2.5 Power consumption Rushton turbine

The power number  $N_p$ , also called the Newton number, is a dimensionless parameter used to relate the power input from the impeller to the fluid properties and rotational speed of the impeller[52][53]. For a stirred single phase vessel the power number is shown in Equation 2.20, in which  $P_o$  is the power input [W],  $\tau$  is the torque on the impeller [ $N \cdot m$ ] and  $\omega$  is the angular velocity[1/s].

$$N_p = \frac{P_o}{\rho N^3 D^5} = \frac{\tau \omega}{\rho N^3 D^5} \quad (2.20)$$

The benefit of correlating the power input with the power number is that the power number for a given geometrical configuration follows the same dependency on the Reynolds number for different tank scales[54]. For low  $Re$ , the power number is inversely correlated to the Reynolds number. But when full turbulence has been realized the power number remains constant[55].

In a multiphase reactor with gas bubbles, the power consumption of impellers is lower with respect to the power consumption at ungasged conditions[56]. A continued trend of power consumption reduction is observed when the gas flow rate is increased[57].

### 3 CFD theory

This chapter covers the theory behind Lattice Boltzmann Equation Method. At first, a brief overview is given about the fundamental theory underlying the method. For a more detailed description of the LBM the reader is referred to book 'The Lattice Boltzmann Method - Principles and Practice' by Krüger et al.[58]. Hereafter it is discussed how M-Star models turbulence and bubbles present in the system. For an extensive overview of the way how M-Star models the LBM the reader is referred to the website of M-Star<sup>2</sup>.

As stated in section 2, the continuity and the Navier-Stokes equations describe the conservation of mass and momentum of a fluid. These set of equations are highly non-linear, and only a few analytical solutions exist under certain circumstances. Therefore it is impossible to directly solve these equations when the encountered problems can become very complex and are often transient. Computational Fluid Dynamics methods provide methods in order to approximate the solutions for the set of equations.

Typically three scales -which are shown in Figure 6- are identified when describing fluids. Namely the microscopic, mesoscopic and macroscopic scale. When describing fluid flow on a microscopic level a look is taken at the scale of individual molecules. The macroscopic level of fluid flow is described by the continuity and Navier-Stokes transport equations which conventional CFD methods discretize in order to approximate the equations. In contrast, the Lattice-Boltzmann CFD method takes a look on the mesoscopic level. This scale is used to describe the distributions of collections of molecules[58].

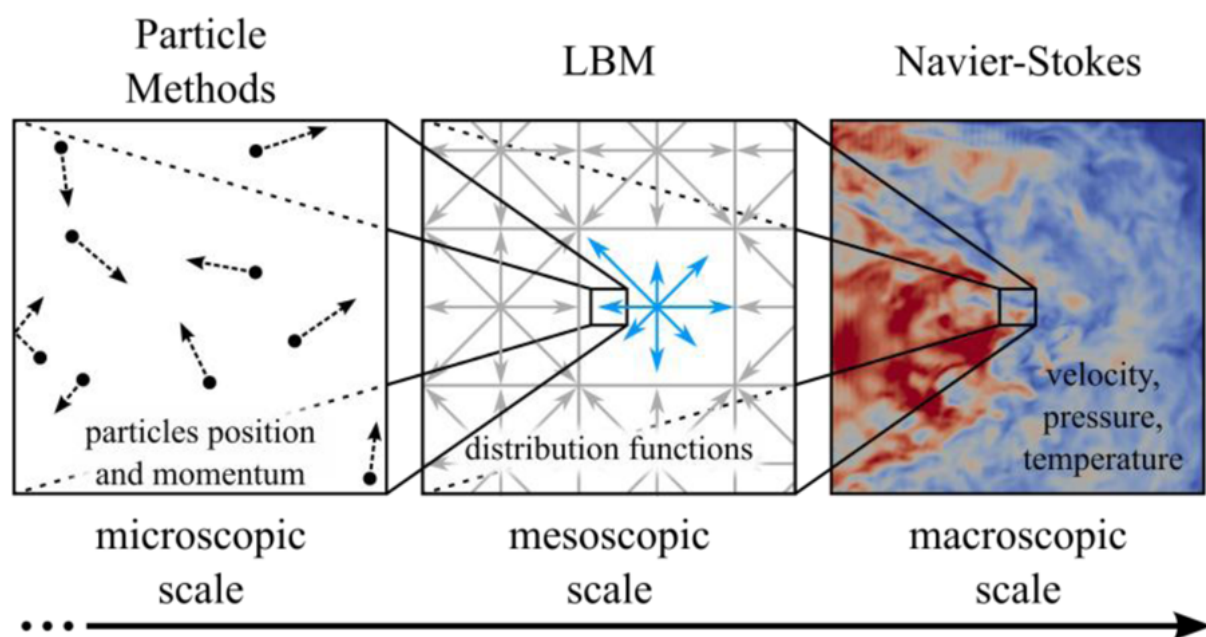


Figure 6: Graphical display of the three scales[59].

#### 3.1 The Boltzmann transport equation

The Lattice-Boltzmann method finds its origin from the kinetic theory of gases[60]. Instead of describing the movement of individual particles, the distribution of particles is described at the mesoscopic scale. The particle distribution function  $f(\mathbf{x}, \boldsymbol{\zeta}, t)$  is the fundamental variable

<sup>2</sup><https://docs.mstar CFD.com/>

which represents the number density of particles with velocity  $\boldsymbol{\zeta} = (\zeta_x, \zeta_y, \zeta_z)$  at position  $\boldsymbol{x}$  and time  $t$ . The particle distribution function  $f$  has the units  $\frac{kg s^3}{m^6}$ . Through its moments, the mesoscopic distribution function is connected with the macroscopic variables such as fluid density  $\rho$  (Equation 3.1) and fluid velocity  $u$  (Equation 3.2).

$$\rho(\boldsymbol{x}, t) = \int f(\boldsymbol{x}, \boldsymbol{\zeta}, t) d^3\boldsymbol{\zeta} \quad (3.1)$$

$$\rho(\boldsymbol{x}, t)\boldsymbol{u}(\boldsymbol{x}, t) = \int \boldsymbol{\zeta} f(\boldsymbol{x}, \boldsymbol{\zeta}, t) d^3\boldsymbol{\zeta} \quad (3.2)$$

The Boltzmann transport equation (Equation 3.3) describes the temporal evolution of the probability density function. In this equation,  $K$  represents an external body force while  $\Omega$  represents the collision operator. This operator describes the rate of change in the particle distribution function due to binary collisions.

$$\frac{\partial f}{\partial t} + \boldsymbol{\zeta} \nabla_{\boldsymbol{x}} f + K \nabla_{\boldsymbol{\zeta}} f = \Omega(f, f) \quad (3.3)$$

Instead of discretizing the continuity and Navier-Stokes equations, like conventional CFD tools do, the Lattice-Boltzmann method discretizes the Boltzmann transport equation. But in order to keep the algorithm manageable, the continuous particle distribution function  $f(\boldsymbol{x}, \boldsymbol{\zeta}, t)$  is transformed into the discrete-velocity distribution function  $f_i(\boldsymbol{x}, t)$  by pre-defining a finite set of velocity vectors. These velocity vectors are transformed into velocity sets by using weighting coefficients  $w_i$  and are denoted by DdQq. The number of velocity vectors is  $q$ , and  $d$  is the number of spatial dimensions in which the velocity set can evolve[58]. Although there are a multitude of different velocity sets, the most commonly used one is D3Q19. This is commonly used for 3D applications as this gives a balanced trade-off between the number of velocities, to minimise memory and computing requirements, and accuracy[61]. This velocity set is shown in Figure 7.

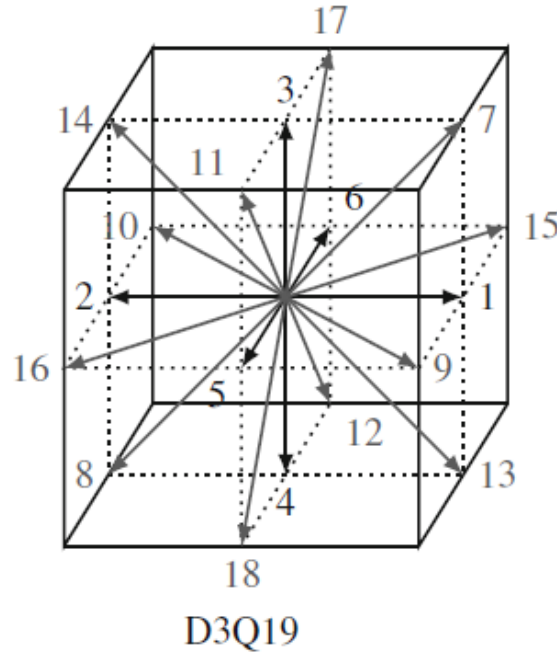


Figure 7: Visual representation of the D3Q19 velocity set[58].

In addition to the pre-defined discrete velocity sets, the discrete-velocity distribution function  $f_i(\mathbf{x}, t)$  has defined points of  $x$  at a square lattice with spacing  $\Delta x$ . Furthermore, a time step  $\Delta t$  ensures that  $f_i(\mathbf{x}, t)$  is defined only at certain times. Together, this discretization of the Boltzmann transport equation in velocity space, physical space and time leads to the lattice Boltzmann equation, shown in Equation 3.4, where it is noted that the term representing the external body force has disappeared. For the sake of simplicity the body force term has disappeared, but when this is needed it can be added to the equation[58]. This equation states how particles move with a certain speed to a neighbouring point at the next timestep, while being affected by the collision operator.

$$f_i(\mathbf{x} + \mathbf{c}_i \Delta t, t + \Delta t) = f_i(\mathbf{x}, t) + \Omega_i(\mathbf{x}, t) \quad (3.4)$$

The collision operator  $\Omega_i$  models particle collisions by redistributing them among the populations at each site. There are a multitude of different operators available, but the most simple and the most commonly used one is the operator by Bhatnagar-Gross-Krook, also called the BGK operator[62].

$$\Omega_i(f) = -\frac{f_i - f_i^{eq}}{\tau} \Delta t \quad (3.5)$$

The BGK operator is shown in Equation 3.5, and models how the populations of molecules relaxes towards an equilibrium  $f_i^{eq}$ . This equilibrium function reflects how the particles represented by the distribution function will reach an equilibrium state when a sufficiently enough time has passed. The equilibrium distribution function follows Maxwellian statistics, and the continuous equilibrium distribution function is shown in Equation 3.6

$$f^{eq} = \rho \left( \frac{m^2}{2\pi RT} \right)^{3/2} e^{-\frac{(\zeta - \mathbf{u})^2 m^2}{2RT}} \quad (3.6)$$

Under the limit of a low local Mach number, a third-order Taylor expansion can be used to recast Equation 3.6:

$$f^{eq} = \frac{\rho}{(2\pi RT)^{3/2}} \exp\left(-\frac{\zeta^2}{2RT}\right) \left( 1 + \frac{\zeta \cdot \mathbf{u}}{RT} + \frac{(\zeta \cdot \mathbf{u})^2}{2(RT)^2} - \frac{\mathbf{u}^2}{2RT} \right) \quad (3.7)$$

which for a system of pre-defined discrete velocity vectors becomes:

$$f_i^{eq} = \omega_i \rho \left( 1 + \frac{\mathbf{u} \cdot \mathbf{c}_i}{c_s^2} + \frac{(\mathbf{u} \cdot \mathbf{c}_i)^2}{2c_s^4} - \frac{\mathbf{u} \cdot \mathbf{u}}{2c_s^2} \right) \quad (3.8)$$

where  $c_s$  denotes the speed of sound.

### 3.2 Algorithm: collision and streaming

The LBE can be divided into two distinct parts which take place in succession: collision and streaming. The full LBGK equation is shown in Equation 3.9 underbracing the collision and streaming part of the equation.

$$\underbrace{f_i(\mathbf{x} + \mathbf{c}_i \Delta t, t + \Delta t)}_{\text{Streaming}} = \underbrace{f_i(\mathbf{x}, t) - \frac{f_i - f_i^{eq}}{\tau} \Delta t}_{\text{Collision}} \quad (3.9)$$

The right hand side of this equation contains the information what is known from the previous time step, and the left hand side represents what is calculated for the next time step. Figure 8 depicts a schematic representation of the collision and streaming steps on a D2Q9 lattice. On the lattice, each lattice node contains  $q$  populations of  $f_i(\mathbf{x}, t)$ . The first slide represents the

varying  $f_i(\mathbf{x}, t)$  values pointing in different directions. The  $f_i(\mathbf{x}, t)$  values are then redistributed according to the collision operator, whereafter the populations are propagated towards the next lattice node. These steps are in principle the same for a D3Q19 lattice. The collision step is an algebraic local operation, while streaming is linear and exact. As collisions take place locally at the lattice nodes, this step is suitable for exploiting GPU hardware by parallingizing the algorithm.

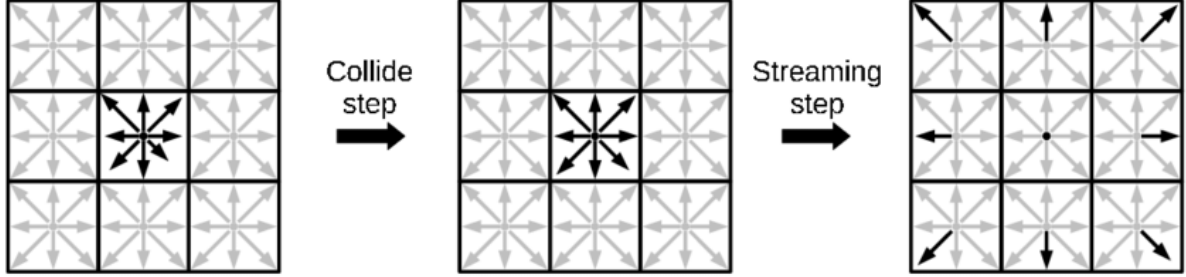


Figure 8: Graphical representation of the collision and streaming step on a D2Q9 lattice[63].

$$f_i^* = f_i(\mathbf{x}, t) - \frac{\Delta t}{\tau} [f_i(\mathbf{x}, t) - f_i^{eq}(\mathbf{x}, t)] \quad (3.10)$$

$$f_i(\mathbf{x} + \mathbf{c}_i \Delta t, t + \Delta t) = f_i^*(\mathbf{x}, t) \quad (3.11)$$

The collision step is shown in Equation 3.10 where  $f_i^*$  represents the post-collision distribution function where the distribution function has received the collision contribution from the collision operator. The streaming step is shown in Equation 3.11, and thus the LBM algorithm is as follows[58]:

1. Compute moments:  $f_i \rightarrow \rho, \mathbf{u}$
2. Compute equilibrium:  $\rho, \mathbf{u} \rightarrow f_i^{eq}$
3. Collide locally:  $f_i, f_i^{eq} \rightarrow f_i^*$
4. Propagate to next neighbours:  $f_i^* \rightarrow f_i$
5. Increment time step & go back to 1

### 3.3 Satisfying the transport equations

Via the Chapman-Enskog expansion the Navier-Stokes can be retrieved by using a perturbation expansion about  $f^{eq}$ [64].

$$f \approx f^{eq} + \epsilon f^{(1)} + \epsilon^2 f^{(2)} + \dots \quad (3.12)$$

Where  $\epsilon$  is small parameter proportional to the Knudsen number (Equation 3.13). The Knudsen number is a dimensionless number which represents the ration between the mean free path ( $\ell_{mfp}$ ) of a particle to the representative length scale of the system. The dependency of the LBM on a small value of Kn through the expansion has the implication that the LBM is only valid when  $\text{Kn} \leq 1$ , meaning that the mean free path between two particles is small compared to the length scale of the physical system. When  $\text{Kn} \geq 1$  the hydrodynamic equations are no longer valid and the kinetic theory description of particles must be used.

$$\text{Kn} = \frac{\ell_{mfp}}{\ell} \quad (3.13)$$

---

The Knudsen number can also be related to the Mach (Ma) and Reynolds (Re) number through the following relationship:

$$Kn = \alpha \frac{Ma}{Re} \quad (3.14)$$

with

$$Ma = \frac{\mu}{c_s} \quad (3.15)$$

In Equation 3.14 and Equation 3.15  $\alpha$  is a numerical constant. When selecting the lattice spacing ( $\Delta x$ ), time incrementation ( $\Delta t$ ) and relaxation time ( $\tau$ ) such that the fluid velocity is much smaller than  $c_s/\sqrt{3}$  (and thus  $Ma \leq 1$ ), it can be shown through lengthy mathematical operations that the solutions of the moments of  $\rho$  and  $\mu$  satisfy the Navier-Stokes equation[65].

### 3.4 Turbulence modelling

Turbulent flow is inherently chaotic due to the non-linearity of the Navier-Stokes equation. When using Direct Numerical Simulations (DNS) even the smallest turbulent scales are modeled exactly, and as such, the size of the lattice spacing must be smaller than this scale[33]. As stated in section 2, the size of the smallest eddies decreases as the Reynolds number increases and thus the amount of lattice units increase significantly at higher Reynolds numbers. Therefore, it is almost impossible to simulate problems relevant to industry as up to billions of grid nodes and millions of CPU hours are needed in order to finish these simulation[66]. In order to solve the turbulent flow field without exactly resolving the Navier-Stokes equations, multiple methods and models are developed in which the smallest scales of turbulence are modeled instead of directly solved.

Within turbulence the fluid velocity can be decomposed in a time-averaged and fluctuating component, shown in Figure 9. This is called Reynolds' decomposition and the subsequent Reynolds-averaged Navier-Stokes (RANS) turbulence model makes use of this decomposition.

The fluctuating component of the fluid flow gives rise to the turbulent phenomena and is depicted in the RANS equation as the Reynolds stress[67]. The Reynolds stress is modelled by a eddy viscosity model which itself is a function of different parameters. Examples of these are the  $k - \epsilon$  and  $k - \omega$  turbulence closure models, in which  $k$  is the turbulent kinetic energy,  $\epsilon$  is the eddy dissipation rate and  $\omega$  is the dissipation rate of the specific turbulent kinetic energy[68].

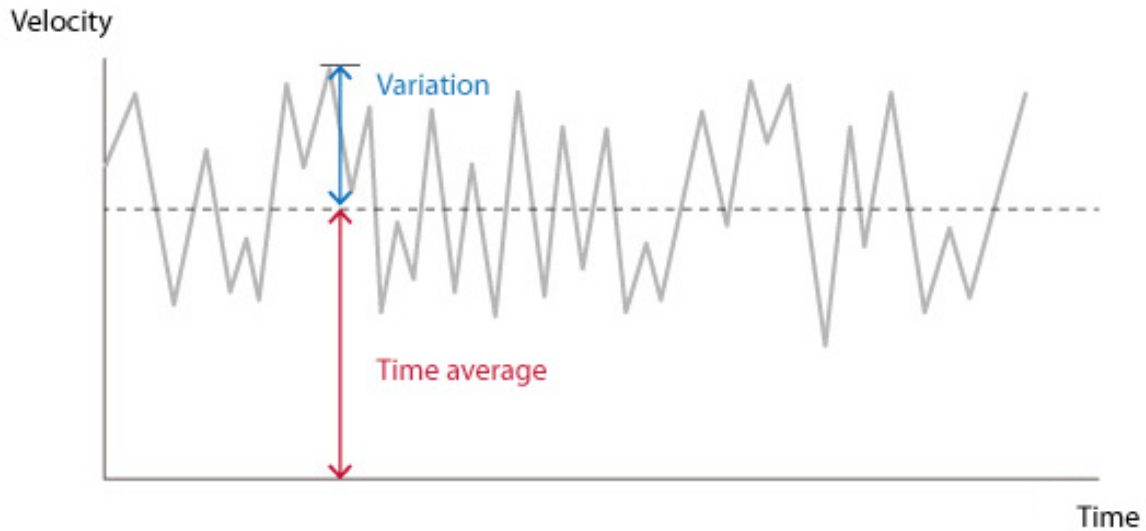
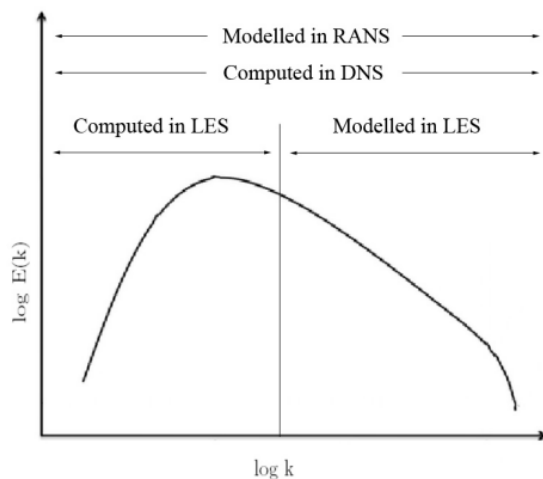
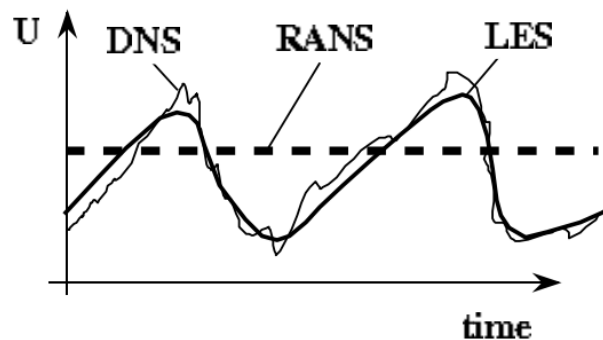


Figure 9: The turbulent fluid velocity can be decomposed in a time-averaged and fluctuating component, taken from <sup>3</sup>.

Another method for solving turbulence is Large Eddy Simulation (LES). Unlike RANS, LES evaluates the mean flow and large, energy containing eddies exactly but in contrast to DNS, it does not simulate the smallest scales of turbulence. Figure 10 shows a graphical comparison between DNS, RANS and LES. Where DNS resolves the fluid velocity and subsequent eddies directly, RANS resolves the Navier-Stokes equation using the time averaged fluid velocity and models the ensuing eddies. LES on the other hand lies in between DNS and LES by computing the largest eddies present in the system and modelling the smallest eddies. For this reason LES is a trade-off between the accuracy of DNS and computational simplicity of RANS[69][70].



(a) Representation of how DNS, RANS and LES model and compute the turbulent eddies[71].



(b) Comparison of how DNS, RANS and LES model the fluid flow velocity[72].

Figure 10: Comparison of DNS, LES and RANS turbulence modelling.

LES resolves the largest eddies while modelling the smallest energy dissipating eddies present

<sup>3</sup>Ueyama, A. (n.d.). Basic Course of Thermo-Fluid Analysis 18: Chapter 5 Basics of thermo-fluid analyses - 5.9.1 Reynolds-averaged Navier–Stokes (RANS), 5.9.2 Large eddy simulation (LES). Cradle CFD. Retrieved January 9, 2023, from <https://www.cradle-cfd.com/media/column/a91>

in the system. This is represented in Figure 11, where above a defined wavelength the eddies are ‘cut’ and not resolved. In this approach, the velocity field is broken down into a filtered and residual component. The filtered velocity can be interpreted as the mean motion of the flow plus the large energy containing scales present in the turbulent field by time- and space averaging, while the unresolved velocity can be seen as the smallest scales present in the system. By ignoring the smallest scales relevant in the system, the computational burden is lessened significantly. In order to still model the effect of the unresolved velocity on the filtered velocity, the molecular viscosity is replaced with an effective viscosity ( $\nu^*$ ) within the momentum transport equations[33].

$$\nu^* = \nu + \nu_t \quad (3.16)$$

In Equation 3.16,  $\nu$  is the molecular viscosity of the fluid and  $\nu_t$  is the sub-grid eddy viscosity, which is computed from:

$$\nu_t = (C_s \Delta_x)^2 \bar{S}, \quad (3.17)$$

where  $C_s$  is the Smagorinsky coefficient and  $\bar{S}$  is the norm of the filtered strain rate tensor, shown in Equation 3.18. By comparing DNS and LES results it was shown that setting the Smagorinsky coefficient to 0.1 delivered the best approximation of DNS when using LES[73].

$$\bar{S}_{ij} = \frac{1}{2} (\partial_j \bar{u}_i + \partial_i \bar{u}_j) \quad (3.18)$$

where  $\bar{u}_{i,j}$  is the filtered velocity component. This model works well for isotropic turbulence but has the shortcoming that it is too dissipative near the walls[33].

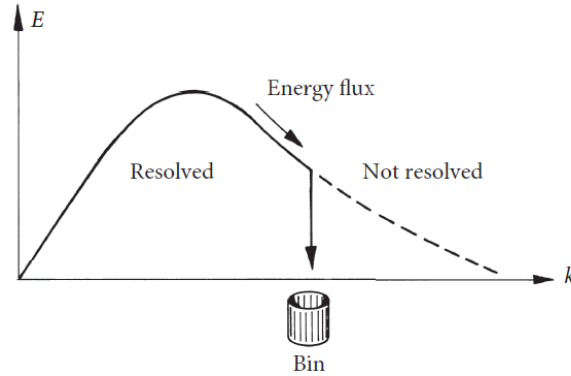


Figure 11: Visual display of the turbulent wavelengths which are not simulated when a Large Eddy Simulation filter is used. The smallest eddies below a certain value are not resolved (visualized by the ‘Bin’), but modeled[33].

As the smallest eddies, which form the bulk of the eddy dissipation rate, are not modeled explicitly when using the LES model, the EDR is broken down into a resolved and unresolved component. Equation 3.19 shows the full energy dissipation rate equation, which is broken down into the resolved (Equation 3.20a) and unresolved (Equation 3.20b) part. As  $\nu_t$  itself is already dependent on the strain rate, the unresolved EDR is related to the third power of the strain rate.

$$\epsilon = 2 (\nu_0 + \nu_t) \sum_{i,j} \bar{S}_{ij} \bar{S}_{ij}, \quad (3.19)$$

$$\epsilon_{\text{res}} = 2\nu_0 \sum_{i,j} \bar{S}_{ij} \bar{S}_{ij} \quad (3.20a)$$

$$\epsilon_{\text{unres}} = 2\nu_t \sum_{i,j} \bar{S}_{ij} \bar{S}_{ij} \quad (3.20b)$$

As most of the energy which dissipates onto the fluid are caused by the smallest turbulence scales present in the system, the unresolved EDR is for most LES simulations orders-of-magnitude larger than the resolved EDR.

### 3.5 Bubble modelling

This section mainly deals with how bubbles are modeled within M-Star, how their trajectories are determined and how bubbles experience break-up and coalescence events. In M-Star, bubbles are modeled as spherical Lagrangian particles that can reside between lattice nodes as they move throughout the geometry, meaning that they are not bound by the discrete nodes of the lattice as the fluid particles are.

#### 3.5.1 Forces on bubble

The bubbles move throughout the vessel according to Newton's second law:

$$m_i \frac{d\mathbf{v}_i}{dt} = \mathbf{F}_i^f + \mathbf{F}_i^c + \mathbf{F}_i^g \quad (3.21)$$

In this equation  $m_i$  is the mass of bubble  $i$ ,  $\mathbf{v}_i$  is the bubble velocity vector,  $\mathbf{F}_i^f$  is the fluid-bubble interaction force,  $\mathbf{F}_i^c$  is a custom user-defined force, and  $\mathbf{F}_i^g$  is the net gravity force acting on the bubble, including buoyancy effects.

The fluid-bubble interaction force is an addition of multiple forces, shown in Equation 3.22. In this equation  $\mathbf{F}_p$  is the pressure force,  $\mathbf{F}_v$  is the virtual mass force,  $\mathbf{F}_s$  is the Safmann lift force, and  $\mathbf{F}_d$  is the drag force.

$$\mathbf{F}_i^f = \mathbf{F}_p + \mathbf{F}_v + \mathbf{F}_s + \mathbf{F}_d \quad (3.22)$$

**Pressure gradient** The pressure force experienced by bubbles arises from pressure gradients in vessel. This includes the effects of buoyancy and gravity[74]. In this equation  $V_P$  corresponds with the bubble volume, while  $\nabla p$  is the experienced pressure gradient.

$$\mathbf{F}_p = -V_p \nabla p, \quad (3.23)$$

**Virtual mass force** The virtual mass force is the force experienced by a bubble as if has an extra mass generated by the acceleration of the particle[75].

$$\mathbf{F}_m = \left( 2.1 - \frac{0.132}{0.12 + A_c^2} \right) V_p \rho_f \left[ \frac{(\dot{\mathbf{u}} - \dot{\mathbf{v}})}{2} \right], \quad (3.24)$$

$$A_c = \frac{(\mathbf{u} - \mathbf{v})^2}{d_p \frac{d(\mathbf{u} - \mathbf{v})}{dt}}, \quad (3.25)$$

**Saffmann lift force** The lift force is the force which acts perpendicularly to the motion of a particle on a particle[75]. This force is usually intended for particles experiencing a low Reynolds particle number<sup>4</sup>.

$$\mathbf{F}_s = 1.61d_p^2\rho_f\sqrt{\frac{\nu_f}{|\omega|}}[(\mathbf{u} - \mathbf{v}) \times \omega_{\mathbf{c}}], \quad (3.26)$$

**Drag force** The drag that bubbles in motion experience is a force in the opposite direction of the motion, and plays a key role in bubble migration throughout vessels[76]. In M-Star, the drag force is modeled as:

$$\mathbf{F}_d = \frac{\pi}{8}C_Dd_p^2\rho_f|\mathbf{u} - \mathbf{v}|(\mathbf{u} - \mathbf{v}), \quad (3.27)$$

in which  $C_D$  is the drag coefficient. There are a multitude of drag coefficient correlations developed to accurately model the drag force. M-Star provides two different options to model the drag coefficient, namely the Free Particle and Packed Bed model. The free particle model is an analytical representation of the drag coefficient developed by Brown and Lawler[77]:

$$C_D = \frac{24}{Re_p}(1 + 0.15Re_p^{0.681}) + \frac{0.407}{1 + \frac{8710}{Re_p}} \quad (3.28)$$

The other option, the Packed Bed model, is the analytical representation of the drag force on a bubble in a packed bed described by Rong, Dong and Yu[78]:

$$C_D = \left(0.63 + \frac{4.8}{\sqrt{Re_p}}\right)\epsilon_f^{(2-\beta)} \quad (3.29)$$

$$\beta = 2.65(\epsilon_f + 1) - (5.3 - 3.5\epsilon_f)\epsilon_f^2 e^{-\frac{(1.5 - \log Re_p^2)}{2}}, \quad (3.30)$$

This drag correlation is mostly applicable to fluidized beds. In both correlations,  $Re_p$  refers to the particle Reynolds number[30]:

$$Re_p = \frac{\rho d_b |u - v|}{\mu} \quad (3.31)$$

For all these equations,  $u$  is the fluid velocity [m/s],  $v$  is the bubble velocity [m/s],  $\rho_f$  is the fluid density [kg/m<sup>3</sup>],  $d_p$  is the bubble diameter [m],  $\nu_f$  is the kinematic viscosity of the fluid [m<sup>2</sup>/s],  $\omega$  is the fluid vorticity [1/s], and  $\epsilon_f$  is the fluid volume fraction [-]

### 3.5.2 Bubble break-up and coalescence

### 3.5.3 Bubble representation

There are two algorithms which can be used in order to model the bubbles, discrete and parcel.

**Discrete approach** In the discrete approach, every bubble is modeled separately and tracked individually throughout the fluid. Bubble break-up and coalescence is modeled explicitly using the approach Reynolds number (Equation 2.13). The value of the approach Reynolds number determines whether bubbles will coalesce (< 40) or bounce off each other. As the amount of bubbles present in an industrial sized reactor can be over billions of bubbles, this approach is limited by GPU memory. Although M-Star mentions that 1 GB of GPU RAM can host up to 25 million bubbles<sup>5</sup>, Thomas et al.[32] mention that approximately 2 million bubbles can be

<sup>4</sup>(2009) Ansys Fluent 12.0 theory guide - 15.2.1 equations of motion for particles. Ansys, Inc. Retrieved January 5, 2023, from <https://www.afs.enea.it/project/neptunius/docs/fluent/html/th/node241.htm#dis-saffman-lift-force>

<sup>5</sup>"Bubbles" M-Star Simulations, LLC, <https://docs.mstar CFD.com/physics/bubbles.html>. Accessed 10 Jan. 2023

tracked by using 1 GB of GPU RAM.

**Parcel approach** With this approach, clusters of bubbles are grouped together inside parcels. These parcels represent the collective motion of a group of bubble which have the same diameter and are influenced by the number scale and the characteristic bubble diameter. The number scale represents the amount of bubbles present in the parcel while the diameter informs the Newtonian trajectory of the bubble. Together these values give the surface area and volume of the cluster and ensure that mass is conserved when the characteristic bubble diameter evolves according to Equation 2.11 instantaneously throughout each time step as the number scale evolves naturally through Equation 3.33 to preserve mass[32].

$$D_p = 0.72 \frac{\sigma^{\frac{3}{5}}}{\rho^{\frac{3}{5}} \epsilon^{\frac{2}{5}}} \quad (3.32)$$

$$N_p^{t+\Delta t} = N_p^t \left( \frac{d_p^t}{d_p^{t+\Delta t}} \right)^3 \quad (3.33)$$

The parcel approach is only valid when the bubble mean free path is small compared to underlying variations in the flow field, as the parcel approach implicitly assumes that break-up and coalescence processes are relatively fast compared to the flow field. Through first principles theory, it can be predicted whether the parcel approach is valid for the given system using Equation 3.34 which predicts the distance a bubble travels before colliding with another bubble, relative to the underlying flow field. As the collision ratio  $R_c$  decreases the parcel approach becomes more valid.

$$R_c \equiv \frac{\ell_m}{\lambda} = \sqrt{\frac{Re}{1080}} \left( \frac{d_b}{\phi T} \right) \quad (3.34)$$

Within this equation,  $\ell_{mfp}$  refers to the mean free path of the bubbles before bubble collision takes place,  $\lambda$  refers to the Taylor scale of turbulence,  $d_b$  is the mean bubble diameter,  $T$  is the tank diameter and  $\phi$  represents the gas hold-up throughout the vessel[32]. It is recognized that the validity of the parcel approach increases as the gas hold-up increases, or the ratio of the mean bubble size with the tank diameter decreases.

### 3.5.4 Fluid-bubble coupling

#### Volume coupling

M-star provides the option to couple the fluid level with the bubble volume. If this is turned off, the fluid level will remain constant throughout the simulation despite an increase in bubble volume when the tank is aerated. If this option is turned on the bubble volume will have an effect on the fluid level throughout the simulation, and as such the lattice domain should be adapted to account for a rise in fluid level.

#### Bubble force coupling

Furthermore, bubbles present in the system have an effect on the turbulent fluid flow field[18]. In M-star the two-way coupling setting provides two algorithms to reflect how bubbles influence the fluid dynamics: density and Third Law.

---

**Density** The Density algorithm is the computational easiest way to account for the effect of bubbles on the fluid flow. This is because the algorithm only considers the effect of buoyancy as a function of the bubble volume fraction on the fluid voxel. This algorithm is suitable if the buoyancy effect on the fluid is much higher than the effect of drag force, which is most of the times realised for bubbles with the size of 1 mm in an agitated tank <sup>6</sup>.

**Third Law** With this approach, all the forces acting on the bubbles is imposed in opposite to the fluid.

---

<sup>6</sup>”Bubbles” M-Star Simulations, LLC, <https://docs.mstarafd.com/physics/bubbles.html>. Accessed 10 Jan. 2023

---

## 4 Computational setup

This chapter introduces the computational set-up used for the simulations. The computer specifications are stated, the geometry of the three cases is presented and the key parameters are discussed. For a complete overview of all the chosen simulation parameters the reader is referred to section 9.

### 4.1 Computer specifications

The simulations were performed on a desktop computer with an Intel(R) Xeon(R) W-2265 CPU, 3.50 GHz and 64 GB installed RAM capacities. Furthermore, a NVIDIA RTX3090 24GB GPU is installed. The Lattice-Boltzmann simulations were conducted using M-Star CFD 3.7.64 (M-Star Simulations, LLC).

### 4.2 Geometry

Three different cases were simulated in order to get insight into the relevant hydrodynamics of (bio-)reactors. In this study, bubbles are modeled using the parcel approach. The first case is a replication of the work done by Thomas et al.[32]. This was done in order to check whether the chosen parameters were a good fit for the next cases. The second case is a computational study on the experimentally obtained bubble size distribution by Barigou[31]. The last case is a study on the hydrodynamics of the industrial sized Stavanger bioreactor. The key geometry sizes are summarized in Table 3, but are elaborated on in the corresponding sections.

Table 3: Geometry of the considered cases

Case number	Symbol	1 (Thomas)	2 (Barigou)	3 (Stavanger)
Tank Diameter (m)	T	0.76	1	2.09
Tank Height (m)	$H_T$	1	1.50	11
Liquid Height (m)	H	0.76	1	6.55
Fluid volume ( $m^3$ )	V	0.35	0.79	22
Impeller Diameter (m)	D	0.305	0.333	0.697
Impeller Clearing Bottom (m)	C	0.234	0.25	1.12
Impeller Spacing (m)	dC	0.291	-	1.46
Sparger Clearing (m)		0.13	0.018	0.47
Sparger Diameter (m)		0.23	0.1	0.4

#### 4.2.1 Case 1: validation case

The reactor of the validation case is shown in Figure 12. The tank is cylindrical and has a diameter of 0.76 m, and a liquid height of 1m, which corresponds to a liquid volume of  $0.35 m^3$ . The bottom of the tank is flat, while the top is open. The tank has four baffles with a width of 0.064 meter and a thickness of 1 mm.

The tank is aerated by a torus-shaped sparger with a clearance of 0.13 m from the bottom of the reactor with a diameter of 0.23 meter. The bubbles are dispersed by two down-pumping Hydrofoil turbines (Catalogued as High Solidity Hydrofoil in M-Star). The bottom impeller has a clearance of 0.234 meter from the bottom, and the top impeller has a clearance of 0.525 meter from the bottom. Both impellers have a diameter of 0.305 meter and rotate with a speed of 150 rpm. Bubbles are fed to the reactor with a rate of 90 L/min with an initial bubble size of 1.5 mm.

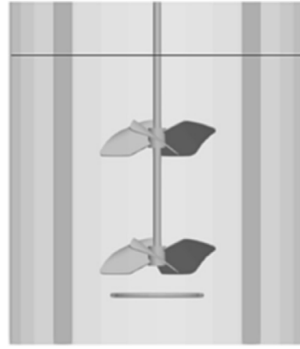
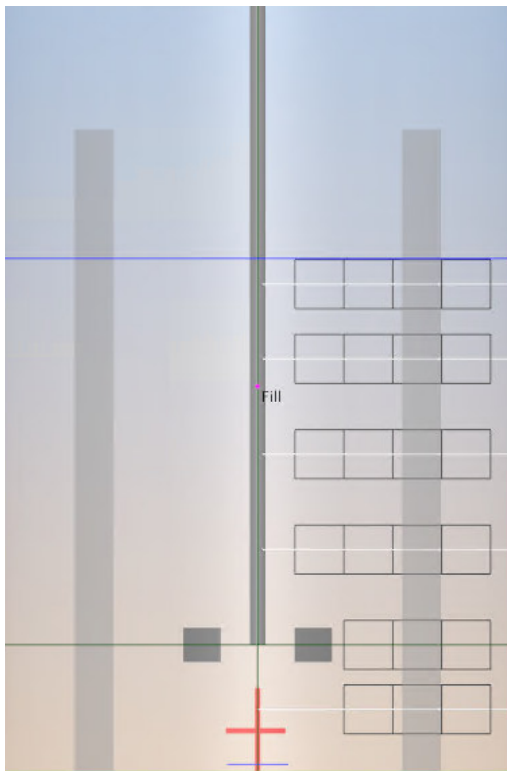


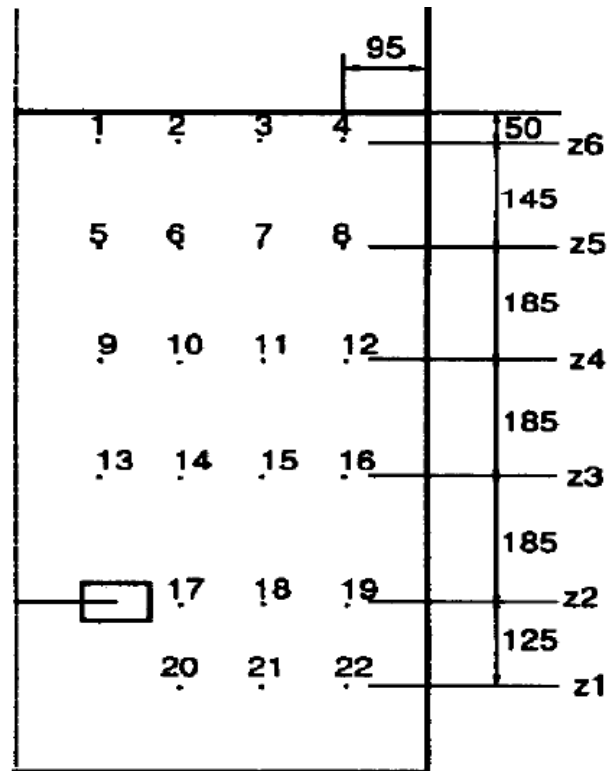
Figure 12: The vessel of the validation case by Thomas et al[32].

A grid spacing of 250 lattice points per vessel diameter ensured grid-independent impeller power number convergence and therefore the results can be considered as independent from grid spacing. The power grid convergence plot can be seen in Appendix C Figure 38. The Courant number was set to 0.1 which ensured a stable simulation.

#### 4.2.2 Case 2: bubble size distribution



(a) Depiction of the builded tank with control volumes.



(b) Position of the measurement probes used for the bubble size distribution experiment in the plane between two baffles(sizes in mm)[31].

Figure 13: Representation of the cross-section of the tank in between two baffles.

Figure 13a depicts the build geometry for the BSD simulations and Figure 13b shows one half of the tank with the specified positions of the probes used during the experiment[31]. The dimensions of the cylindrical tank with a flat bottom are shown in Table 3. The tank was

agitated by a standard Rushton turbine with six blades, and a torus shaped sparger provided the aeration. The tank has four baffles on the side ranging from top to bottom with a width of 0.1 m and thickness of 7 mm. As the main task of this case was to investigate the bubble size distribution, it was chosen to set up 22 Control Volumes (CVs) in order to get the distribution at the respective locations in the tank. The CVs have sides with a length of 0.095m, corresponding to a volume of 0.857377 L. The middle of the cube corresponds with the location of the probes in the experiments. Furthermore, output lines have been set up through the middle of every row of control volumes, in order to get better insight into the relevant hydrodynamics for the bubble size distribution. A resolution of 250 lattice points across the vessel diameter and a Courant number of 0.05 ensured a grid independent impeller power number and stability.

As to compare the suitability of the LBM, and the influence of agitation rate and gas flow rate on the obtained numerical results, twelve cases which consisted of three different gas flow rates with varying agitation speeds were performed and compared with the experimentally obtained results of Barigou[31]. The specific agitation rates for the three varying gas flow rates are shown in Table 4 together with the injection scale. The injection scale is the number of modeled bubbles which are initially represented by one parcel. It has been shown that, although the computational burden is lessened significantly, the order-of-magnitude of the injection scale has no large influence on the amount bubbles modeled if the discrete model was to be used.

If the mean bubble diameter would be 0.5 mm for a gas hold-up of 11.45%, the total amount of bubbles present in the system would be 172 million. As such, the discrete approach could potentially be used to simulate this particular case according to M-Star. However, Thomas et al. mention that, instead of 25 million bubbles, only 2 million bubbles can be tracked with 1 GB of GPU RAM. Even if 1 GB of RAM is capable of tracking 25 million bubbles, the discrete approach would require a significant amount of computational time to complete, and this was considered unfeasible for the current case.

Table 4: Specifications of the twelve different cases

Gas Flow Rate	Injection Scale	RPM	RPM	RPM	RPM
0.00164 [ $m^3/s$ ]	20	100	150	280	250
0.00438 [ $m^3/s$ ]	50	130	180	270	300
0.00687 [ $m^3/s$ ]	75	180	200	285	385

The validity of the parcel approach can be assessed by using Equation 3.34. The parcel approach becomes increasingly valid as  $R_C$  decreases. For an agitation speed of 100 RPM, and a GFR of  $0.00164m^3/s$ , the experiments indicate a gas hold-up of 1.91%. By estimating a mean bubble diameter of 3 mm, which is most probably an overestimation,  $R_c$  will be 2.07 and thus the mean free path of the bubble is order-of-magnitude consistent with variations in the turbulent flow field. For an agitation speed of 385 RPM, and a GFR of  $0.00687m^3/s$ , the experiments indicate a gas hold-up of 11.45%. For  $R_C$  to reach unity, the mean bubble size should be 4.46 mm. This is a larger mean diameter than the experimental results indicate, and as a smaller bubble size would result in a lower  $R_C$ , the parcel approach is also applicable in this case. By examining these two cases it is determined that the parcel approach is indeed valid for this simulation.

### 4.2.3 Case 3: industrial sized Stavanger bioreactor

This case consisted of a cylindrical tank with a flat bottom, agitated by Rushton turbines and aerated by a torus-shaped sparger. The dimensions and spacing of the impellers and sparger are shown in Table 8. The tank has four baffles across the walls with a width of 0.1672 m and thickness of 1 cm. Output lines were placed along every impeller height to gain insight into the EDR generated by the impeller. A resolution of 240 lattice nodes across the tank diameter and

a Courant number of 0.04 ensured a converged grid with stability with a reasonable computational speed.

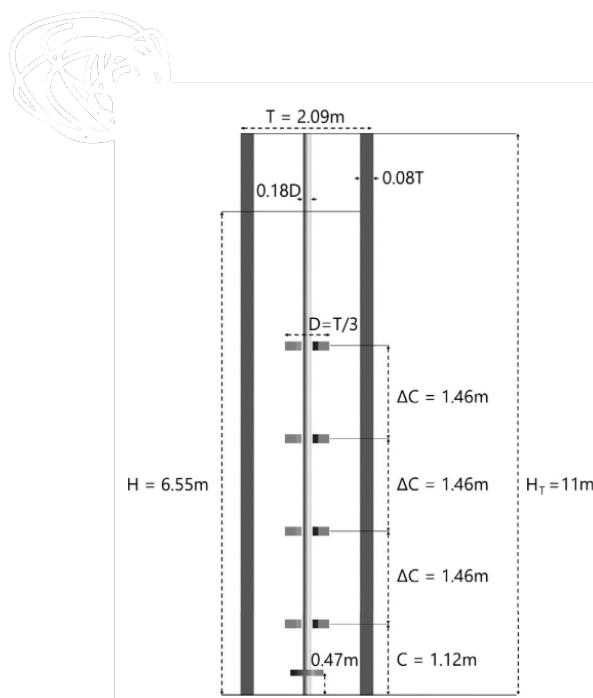


Figure 14: Geometry of the Stavanger case[26]

Twelve main (sub)cases were simulated with varying gas flow rates and agitation rates. The four agitation rates are 0, 100, 115 and 133 RPM. The three gas flow rates with corresponding used injection scales are shown in Table 5. The experimental data indicates that a gas hold-up of 7.7% is expected for an agitation rate of 100 RPM and a GFR of 2700 L/min. For  $R_C$  to be unity, the mean bubble diameter should be 5.88 mm. As such, the parcel approach is valid for the industrial-scale case.

Table 5: Injection scales used for the parcel approach for the different gas flow rates.

Gas Flow Rate [L/min]	Injection Scale
2700	5000
5400	10000
10800	20000

### 4.3 Universal parameters

All simulations were performed with the free surface fluid model. This model is needed when simulating multiphase cases. The interface between the liquid and the atmosphere above the gas (or headspace) is the free surface. For turbulence modelling the LES model with a Smagorinsky coefficient of 0.1 was used[73].

**Physical Properties** The density of the fluid -water, a Newtonian fluid- was set to  $1000 \text{ kg/m}^3$  with a kinematic viscosity of  $10^{-6} \text{ m}^2/\text{s}$ . The headspace pressure was set to 101325 [Pa] and a surface tension of 0.072[N/m] was applied between the fluid and bubbles. The bubbles enter the vessel with a density of  $1.2 \text{ kg/m}^3$  and an initial diameter of 1.5 mm. The

---

hydrostatic effects on the bubble size are not considered as this is not supported for the parcel approach.

**Forces, Break-up and Coalescence** As the case of Thomas et al.[32] was used to validate the current approach, their enabled forces acting on a bubble were used. As such, the gravity, buoyancy and virtual mass forces were turned on. For the drag force the FreeParticle model was used and the bubble was two-way coupled with the fluid via Newton’s third law. When bubbles encounter a solid object, the bounce back option was used. Break-up and Coalescence were turned on, while the parcel representation was used with the UnifiedModel as Breakup model. A maximum coalescence diameter of 1 cm was enforced, with a deletion parameter of  $10^{-5}$ . The Third Law Numerical Scaling was kept on the default of 0.5.

**Boundary Conditions and Wall Interaction** The boundary conditions were set to NoSlip with the exception being the top of the vessel where the FreeSlip boundary condition was set.

The wall boundary type was set to interpolated, rather than grid-aligned, implying that the effects of the wall on the fluid particles are extrapolated as a function of distance from the wall. This approach should be superior when using curved walls. Wall functions can be implemented to account for the over-estimation of the EDR near walls when using LES simulation[79]. For simulation stability the wall function was turned off, meaning that no model was used in order to satisfy the physics near the wall<sup>7</sup>. The fluid Interaction was turned on such that interactions between the fluid and wall are enabled. The internal mass of the impellers were neglected when the forces on the fluid were calculated. It was shown that the ommittance of a wall function has little impact on simulations by Haringa[80]

#### 4.3.1 Free Ssurface interaction

All bubbles which come in contact with the free surface are removed from the simulation. However, there was an issue where bubbles became trapped under the free surface, shown in Figure 15. Because of this, the liquid level kept on rising as more and more bubbles accumulated in the vessel until a 'breaking point' was reached where suddenly all the bubbles under the free surface disappeared and the cycle of accumulation and removal continued. Therefore the bubble removal volume fraction was set to 0.1 to ensure that bubbles are removed when in contact with the free surface. This implicates that, when the liquid volume fraction reaches a value of 0.1, bubbles are removed from the simulation in that specific voxel. However, setting the removal fraction could have an impact on accumulation of bubbles within the vessel itself.<sup>8</sup>

---

<sup>7</sup>(2020) What is y+(yplus), SimScale, Retrieved: December 27, 2022, from [simscale.com/forum/t/what-is-y-plus/82394](https://www.simscale.com/forum/t/what-is-y-plus/82394)

<sup>8</sup>The solution of setting a removal factor was recommended by M-star in order to circumvent the accumulation issue. They had never seen this glitch before and claim that the issue is over with an update of the software.

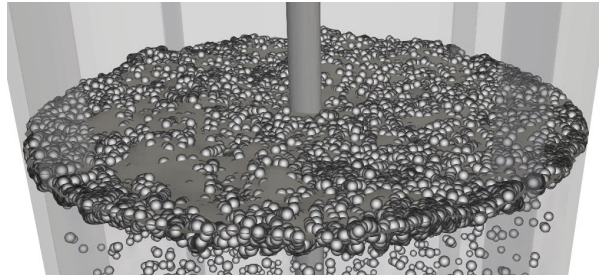


Figure 15: Bubble accumulation at the free surface. Instead of leaving the system when reaching the free surface, the bubbles become 'trapped' underneath.

## 5 Results - validation and bubble size distribution

This chapter covers the results of the validation case and BSD case, while simultaneously discussing the results. The volume of these cases were of lab-scale.

### 5.1 Validation case - lab scale

Figure 16 shows the amount of bubbles present in the system as a function of time. As can be expected, the amount of bubbles fluctuate heavily although on average a steady state is reached. Although the amount of bubbles present in the system still increases a bit after 45 seconds, the system is considered to be in steady state and it is not expected that it affects the average of bubbles present in the system significantly. In addition, the gas hold-up does increase slightly from  $t = 45\text{s}$ , while the mean bubble diameter decreases slightly. To verify whether the simulation has indeed reached a steady state, the simulation time was extended. As expected, the amount of bubbles present in the system dropped again. This is shown in section 10.

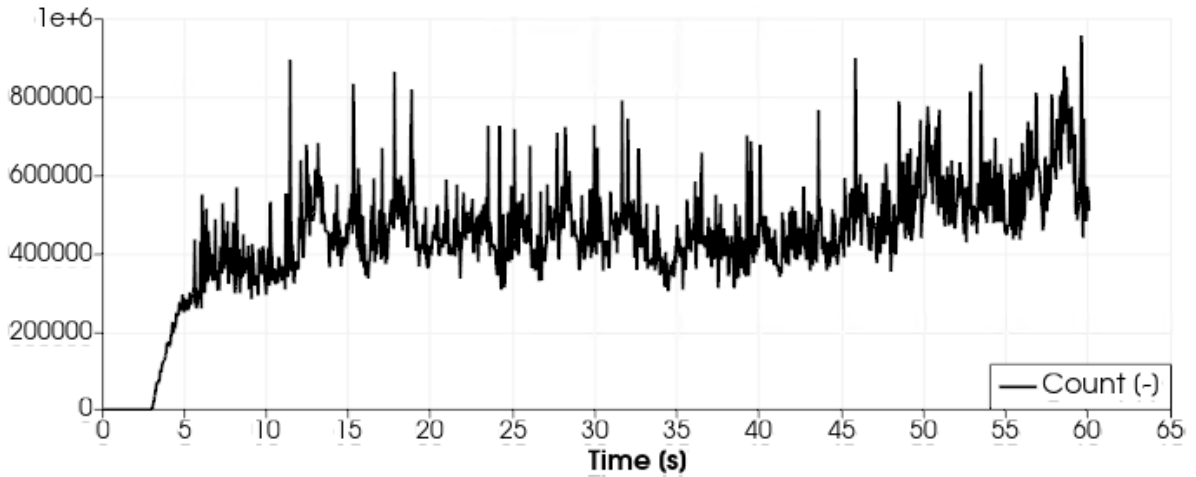


Figure 16: Bubble count for the validation case.

The values for the bubble count, mean bubble diameter and gas hold-up are shown in Table 6 and are obtained by time-averaging from  $t = 30\text{-}60$  seconds. On average, the amount of bubbles present in the system after reaching steady state is 496 thousand bubbles (496,922). This is in line, although slightly lower, than the 503,000 thousand bubbles mentioned in the article when using the discrete approach. The mean diameter  $d_{10}$  of the bubble size is 1.3mm vs 1.26mm. The gas hold-up is 0.87% vs mentioned 1%. The chosen parameters and parcel approach give a slight under-prediction of the gas hold-up and amount of bubbles present in the system, but it is considered to be in the acceptable range.

Table 6: Comparison between values obtained by the discrete bubble representation and parcel representation. The values are time-averaged from  $t = 30\text{-}60$  seconds. The values for the discrete representation are taken from Thomas et al.[32].

	Discrete (Paper)	Parcel (Verification)
Bubble Count (-)	503,000	496,922
Mean Bubble Diameter (mm)	1.2	1.26
Gas Hold-up (%)	1	0.87

A thing to note is that the article does not specify at which time-step they start to average

the values of the bubble count, bubble diameter and gas hold-up, which could influence the comparison between the results. For example, if time-averaging was started after 45 seconds, the average amount of bubbles present would be 558,904, which is an over-prediction compared to the discrete approach, but almost similar to the the 557,000 bubbles mentioned in the article when using the parcel approach. Furthermore, the mean diameter of the bubble would be 1.20 mm if time averaged after 45 seconds while the gas hold-up would be 0.89 %. The values of the gas hold-up and mean bubble diameter are not specified for the parcel approach conducted by Thomas, so those values cannot be compared to the current work.

## 5.2 Case 2: lab-scale tank (BSD)

### 5.2.1 Gas hold-up

The gas hold-up values for the experimentally obtained results and LBM predictions are displayed in Table 7. Although the gas hold-up increases as the agitation speed or the GFR is increased, the predicted values of the gas hold-up are too low compared with the experimental data. When comparing the gas hold-up for all the cases, it is seen that M-star consequently predicts the gas hold-up with a factor of 3-5 times too low. And as such, the amount of bubbles present in the vessel or the residence time too low. There are multiple reasons why the residence time could be too low. If the size of the modeled bubbles is too large, they will leave the vessel faster when compared to smaller bubbles due to buoyancy[81]. The drag force is another force which plays a key role in the residence time of bubbles[82]. If the drag force is modeled incorrectly the residence time of the bubbles, and thus the gas hold-up, could deviate significantly.

Table 7: Gas hold-up comparison for the experimental obtained values and the LB CFD results

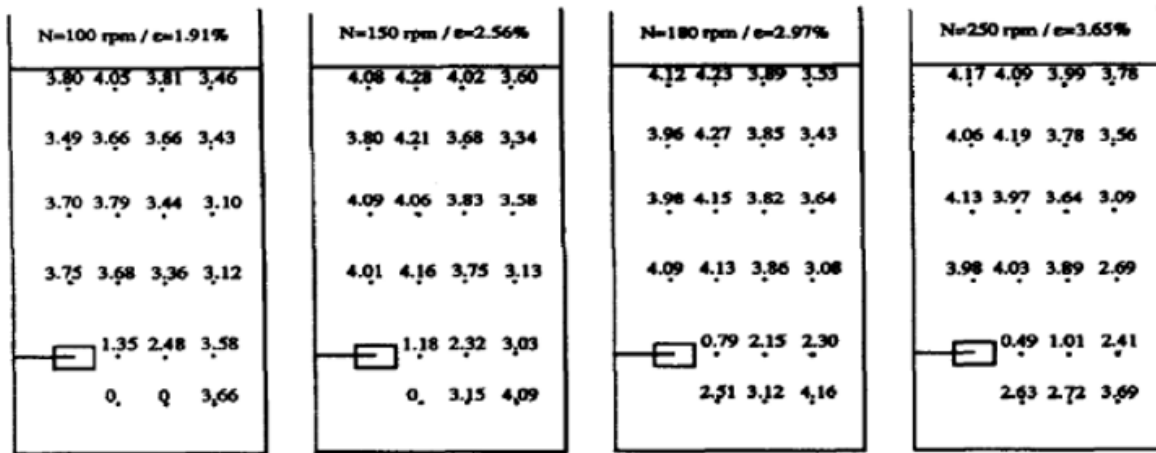
GFR ( $m^3/s$ )	RPM	100	150	180	250
	0.00164	Exp	1.91 %	2.56 %	2.97 %
CFD		0.41 %	0.47 %	0.50 %	0.58 %
RPM		130	180	270	300
0.00438	Exp	5.12%	6.10%	6.99%	7.51%
	CFD	1.20%	1.29%	1.57%	1.66%
	RPM	180	200	285	385
0.00687	Exp	7.72%	7.78%	9.56%	11.45%
	CFD	2.02%	2.05%	2.52%	2.90%

### 5.2.2 Bubble size distribution

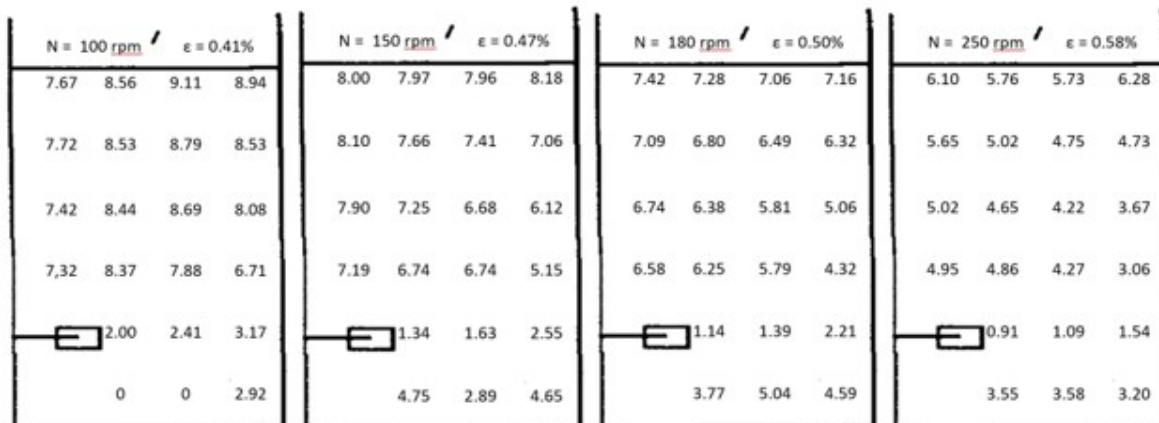
Figure 17, Figure 18 and Figure 19 shows the experimentally obtained Sauter mean diameter and the numerically obtained mean diameter at different positions in the tank for respectively 0.00164  $m^3/s$ , 0.00438  $m^3/s$  and 0.00687  $m^3/s$  with different agitation speeds. What must be noted in advance is that the experimentally obtained bubble size distribution represents the Sauter mean bubble diameter  $d_{32}$ , while the numerically obtained distribution shows the mean bubble size characterized  $d_{10}$ . Unfortunately M-star does not provide the option to register the Sauter mean diameter, and therefore it was chosen to represent them in this way. Although in general the  $d_{32} > d_{10}$ , the differences should not be too large[47]. Nevertheless, if the  $d_{32}$  bubble size was acquired from the simulations, the over estimation of the mean bubble size would be larger.

In line with the experimental data, the smallest bubble sizes are found in the region next to the impeller. This is due to the generated turbulence which is the highest close to the impeller. As the agitation speed is increased, turbulent kinetic energy generated by the impeller becomes larger and the bubbles tend to become smaller at the impeller plane.

(a)  $Q = 0.00164 \text{ m}^3/\text{s}$



(a) Experimental results.



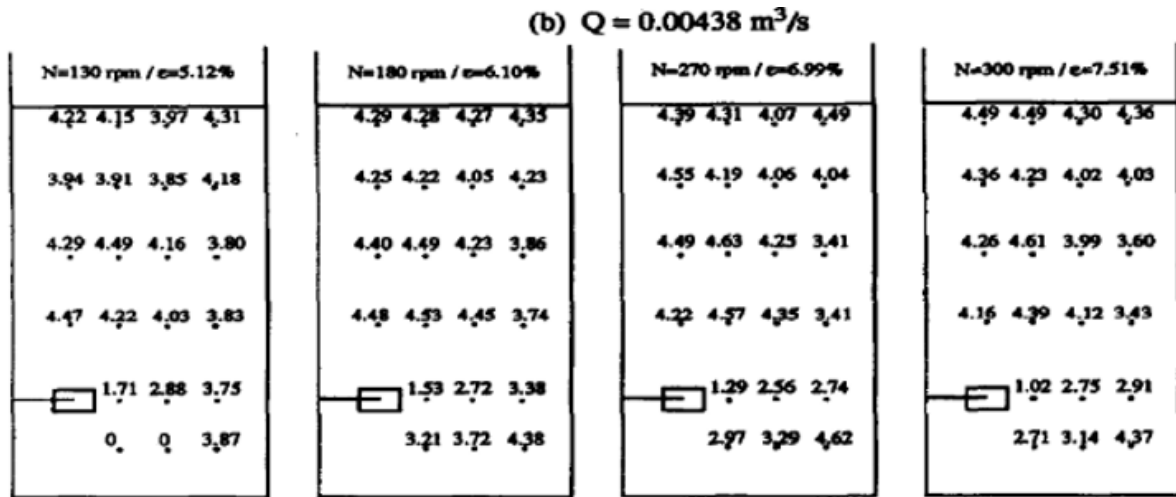
(b) LB-CFD results.

Figure 17: Comparison of the obtained bubble size distribution at a gas flow rate of  $0.0164 \text{ m}^3/\text{s}$ . The top row reflects the experimental data, the bottom row the CFD results.

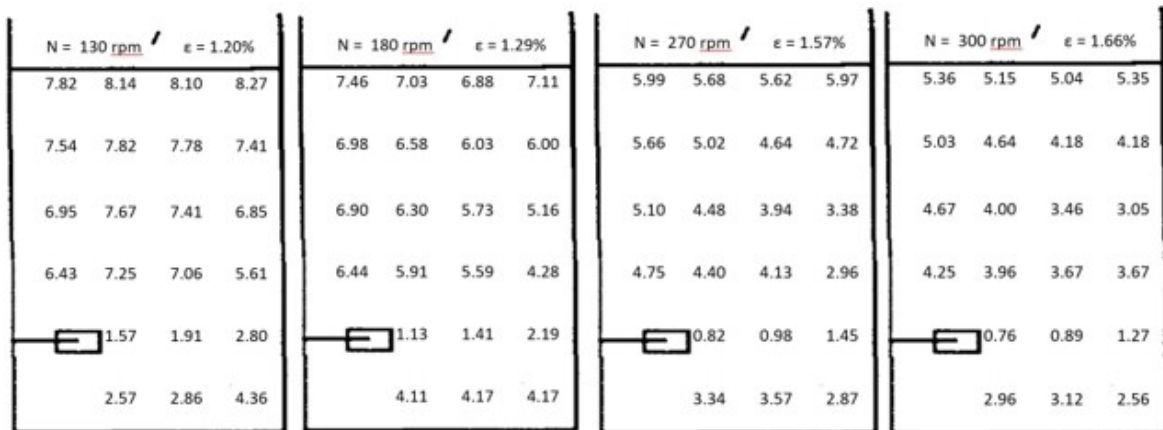
When considering the data of Figure 17, the simulation predicts a loading regime for an agitation speed of 100 RPM as there are no bubbles present in the region underneath the impeller, which is in line with the experimental data. According to the acquired BSD for an agitation speed of 150 RPM, the bubble are dispersed throughout the vessel, which contradicts the experimental data. However, this discrepancy could be due to the size of the control volumes which were set up, while in the experiment a capillary probe was used to determine the size of the bubbles. While the capillary acquires the BSD at a specific point in the vessel, the CV's acquire the size of the bubbles in a volume of 0.86 L which could influence the results.

When focusing on the bubble sizes at the control volumes, it is observed that in the region next to the impeller the bubble sizes are close to the sizes of the experiment, with the control volume right next to the impeller predicting a too high bubble size, and the next regions being marginally smaller than the experimental values. The regions above the impeller show a larger

offset between the experimental values and the numerical values, with the numerical value being predicted with a factor of roughly two too high. Bearing in mind that  $d_{10} < d_{32}$ , it can be deduced that the bubble size distribution in the area above the impeller plane is not predicted properly when compared to the experimental BSD. However, the offset does diminish as the agitation speed is increased.



(a) Experimental results.



(b) LB-CFD results.

Figure 18: Comparison of the obtained bubble size distribution at a gas flow rate of  $0.0438 \text{ m}^3/\text{s}$ . The top row reflects the experimental data, the bottom row the CFD results.

The experimentally and computationally obtained bubble size distributions for a gas flow rate of  $0.00438 \text{ m}^3$  are portrayed in Figure 18. For an agitation speed of 130 RPM the CFD results predict fully dispersed hydrodynamics while the experimental results reflect a loading regime, but as before this could be due to the size of the control volumes. As before, the BSD in the impeller plane are closest to the BSD obtained by the experiment while the area above the impeller plane display bubble sizes larger than experimentally obtained. Furthermore it is observed that the bubble sizes tend to become smaller as the agitation speed is increased, with the BSD at an agitation speed for 250 RPM nearing the BSD obtained by Barigou.

(c)  $Q = 0.00687 \text{ m}^3/\text{s}$ 

$N=180 \text{ rpm} / \epsilon=7.72\%$	$N=200 \text{ rpm} / \epsilon=7.78\%$	$N=285 \text{ rpm} / \epsilon=9.56\%$	$N=385 \text{ rpm} / \epsilon=11.45\%$
4.31 4.18 4.19 3.95	4.26 4.16 4.21 3.60	4.07 4.34 3.90 3.45	4.30 4.27 3.86 3.46
4.14 4.39 4.37 4.41	4.07 4.28 4.38 4.43	4.10 4.13 3.98 4.10	4.14 4.14 3.98 3.77
4.55 4.47 4.41 4.13	4.38 4.47 4.44 3.95	4.19 4.17 4.42 3.68	3.94 3.81 3.97 3.37
4.56 4.44 4.42 3.71	4.52 4.63 4.43 3.76	4.42 4.47 4.34 3.51	4.15 4.23 4.11 3.20
 2.10 3.29 3.44	 1.97 3.03 3.30	 1.62 3.70 3.38	 1.41 3.95 3.44
$Q$ 3.56 4.35	$Q$ 3.68 4.59	3.01 3.40 4.42	2.82 3.18 4.02

(a) Experimental results.

$N = 180 \text{ rpm} / \epsilon = 2.02\%$	$N = 200 \text{ rpm} / \epsilon = 2.05\%$	$N = 285 \text{ rpm} / \epsilon = 2.52\%$	$N = 385 \text{ rpm} / \epsilon = 2.90\%$
7.28 6.78 6.90 7.11	6.65 6.56 6.43 6.78	5.85 5.23 5.02 5.52	4.42 4.06 3.93 4.23
6.80 6.57 6.28 6.09	6.78 6.31 5.90 5.70	5.35 4.74 4.26 4.14	4.13 3.50 3.19 3.09
6.50 6.20 5.72 5.12	6.18 5.69 5.10 4.62	4.81 4.36 3.83 3.26	3.54 3.12 2.75 2.35
6.37 5.95 5.31 4.14	5.67 5.42 5.04 3.86	4.46 4.32 3.94 2.71	3.25 3.11 2.88 1.93
 1.11 1.38 2.18	 1.02 1.27 2.05	 0.79 0.96 1.36	 0.58 0.69 0.95
3.58 4.43 4.51	3.70 4.39 4.06	3.18 3.30 2.66	2.32 2.39 1.99

(b) LB-CFD results.

Figure 19: Comparison of the obtained bubble size distribution at a gas flow rate of  $0.0687 \text{ m}^3/\text{s}$ . The top row reflects the experimental data, the bottom row the CFD results.

The cases with the highest gas flow rate,  $0.00687 \text{ m}^3/\text{s}$ , are shown in Figure 19. These cases also feature the largest set of agitation rates, with a minimum of 180 rpm and a maximum of 385 rpm. The first thing which is noted is that the dispersion of the bubbles is not properly predicted for the cases with an agitation rate of 180 rpm and 200 rpm, as it is predicted that the bubbles are completely dispersed which is not supported by the experimental data. The CFD bubble sizes at the impeller plane predict bubble sizes which are lower than the experimental bubble sizes. Keeping in mind that the CFD data reflects the  $d_{10}$  values and the experimental data the  $d_{32}$  values, this could imply that at a higher gas flow rate the bubble sizes at the impeller plane are a better fit to the experimental data, although it is impossible to make a quantitative conclusion based on this observation. When considering the region above the impeller, the bubble sizes are still predicted to be too high for the agitation rates of 180, 200 and 285 RPM. Interestingly, the BSD for an agitation rate of 385 RPM is remarkably close to the experimental data. At almost every position the bubble sizes are predicted to be lower than the experimental values, with the exception being at the interface between the fluid and the head space.

The only agitation rate present for the three different aeration rates is 180 RPM. A higher gas flow rate leads to more coalescence events and thus a higher bubble size, and is supported by

the experimentally obtained BSD. However, this is not the case for the obtained BSD by using the LBM simulations, where the bubble sizes decrease (albeit not significantly) when the aeration rate is raised at the same agitation speed. Considering an uncertainty in bubble size determination by using CV's and the current approach, the aeration rate has no significant influence on the bubble sizes although increasing the gas hold-up in the vessel. The most probable reason for the aeration rate having no effect on local bubble size is the usage of the parcel approach when modelling the bubbles. In this approach, the bubble diameter evolves instantaneously according to Equation 2.11 as a function of the local eddy dissipation rate  $\epsilon$ . As bubble coalescence is temporal restricted, the assumption of instantaneous evolving of the bubble diameter could lead to a significant deviation.

### 5.2.3 Eddy dissipation rate

The dimensionless eddy dissipation rate ( $\bar{\epsilon}$ ) against the normalized diameter of the tank ranging from tip of the impeller to the wall was measured at the impeller output plane. This is shown in Figure 20 for an agitation speed of 180 RPM and 385 RPM. The EDR measured at all the output lines for these cases can be found in section 8. This was done in order to compare the computed  $\epsilon$  with the dimensionless analysis of Wu and Patterson[83] and the experimental obtained values by Ducci and Yianneskis[84]. They obtained experimentally obtained values for  $\epsilon$  by using laser Doppler anemometry (LDA) and Particle Image Velocimetry (PIV) measurements[84]. Both cases show the same profile for  $\bar{\epsilon}$ , which is expected. The LES simulation underestimates the EDR near the impeller when comparing it to the values obtained by Ducci et al.[84], while it does give a good agreement with the dimensionless analysis of Wu and Patterson[83] at a further distance from the impeller. The underestimation of  $\epsilon$  was also mentioned by Hartmann et al.[85] and Derksen et al.[86] when using LES models with a Smagorinsky coefficient of 0.1. The underestimation of the EDR at the impeller wake implies that the smallest eddies are not correctly captured by the model, which could have implications for the equilibrium diameter of the bubbles as it is correlated to the EDR (Equation 3.6). Studies have shown that setting the Smagorinsky coefficient to 0.2 could lead to a better agreement of  $\epsilon$  with experimental data[87][88].

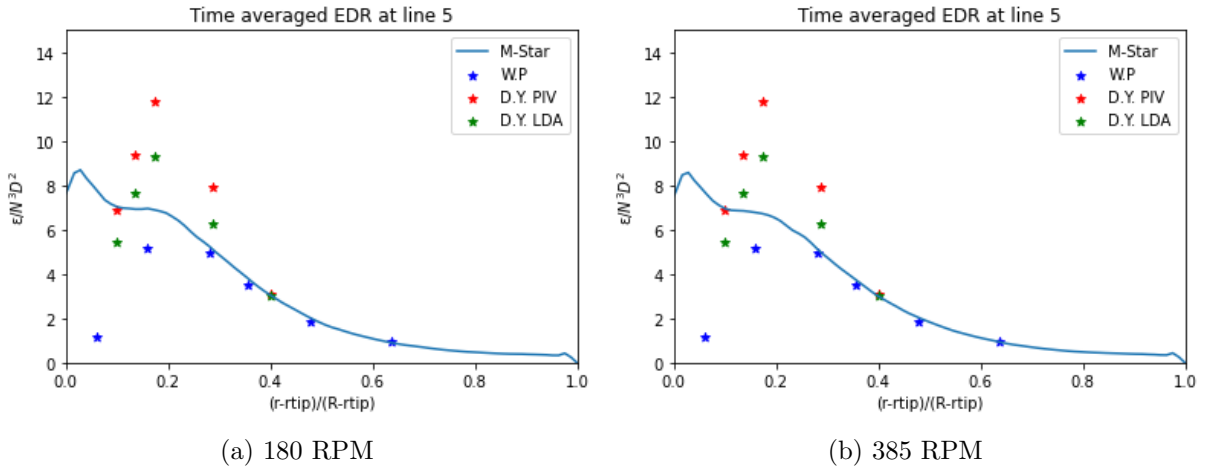


Figure 20: Non-dimensionalisation of the eddy dissipation rate. Abbreviations: W.P = Wu Patterson[83], D.Y = Ducci and Yianneskis[84].

### 5.2.4 Influence of the maximum coalescence diameter parameter

Three additional simulations were conducted with a maximum coalescence diameter of 5mm instead of 10 mm, ensuring that the bubble size distribution was more in line with the experi-

mental data. The BSD for an agitation speed of 180 RPM at different gas flow rates are shown in Figure 21. When a maximum coalescence diameter of 5 mm is enforced, the bubble size distribution throughout the vessel agrees better with the experimental data. The gas hold-up, in contrast, only improves marginally and the effect of the maximum coalescence diameter on the hold-up is negligible in these cases.

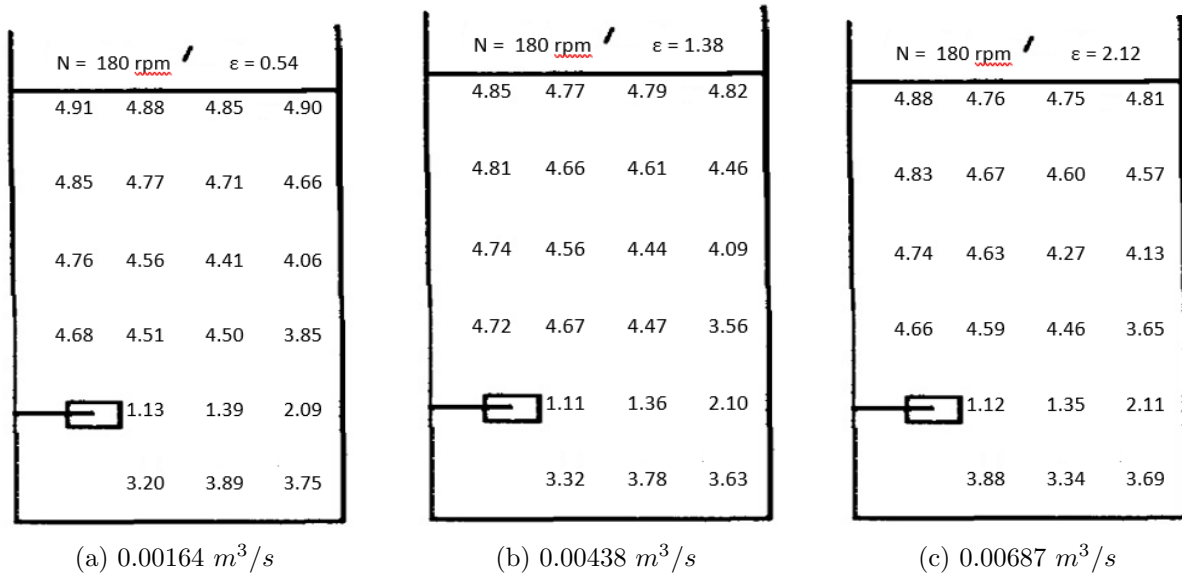


Figure 21: Comparison of the influence of the specified max coalescence diameter for an agitation rate of 180 RPM for the three specified gas flow rates. In these cases, a maximum coalescence bubble size of 5mm was enforced instead of 10mm. Although the bubble size distribution in the vessel is more in line with the experimental data, the estimated gas hold-up does not improve with respect to the experimental data.

### 5.2.5 Contour plots

The contour plot of the gas fraction at an agitation speed of 180 RPM and GFR of  $0.00164 \text{ m}^3$  is shown in Figure 22. The axis is scaled from 0-2.5% where the red spots indicate regions with a gas hold-up higher than 2.5%. The bulk of the vessel contains a gas hold-up lower than 1%, which is coherent with the gas hold-up in the vessel being 0.50%. As expected, the bubbles are weakly dispersed throughout the vessel, with a weak re-circulation pattern underneath the Rushton impeller. The gas hold-up is the largest at the walls of the tank (when disregarding the gas hold-up above the sparger).

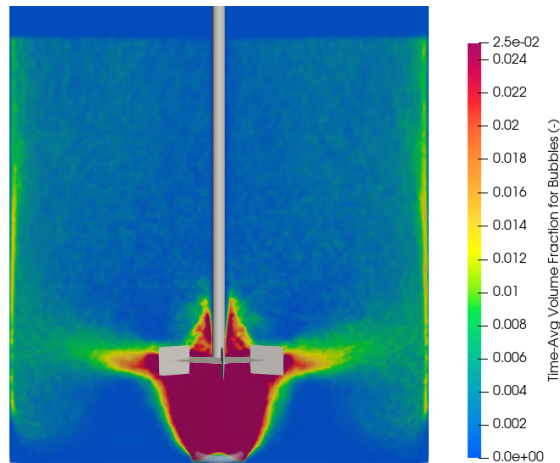


Figure 22: Contour plot of the gas fraction for an agitation speed of 180 rpm and GFR of  $0.00164 \text{ m}^3/s$ . The axis is scaled from 0-2.5% gas hold-up. The dark red spots indicate regions where the gas hold-up exceeds 5%.

A stronger recirculation pattern underneath the impeller plane is acquired when increasing the agitation speed to 385 RPM. The contour plot for such an agitation rate with a GFT of  $0.00687 \text{ m}^3/s$  is displayed in Figure 23. This axis is scaled from 0-10%, where the dark red spots indicate a gas hold-up exceeding 10%. As before, the gas hold-up is significantly higher at the tanks walls then in the bulk of the fluid.

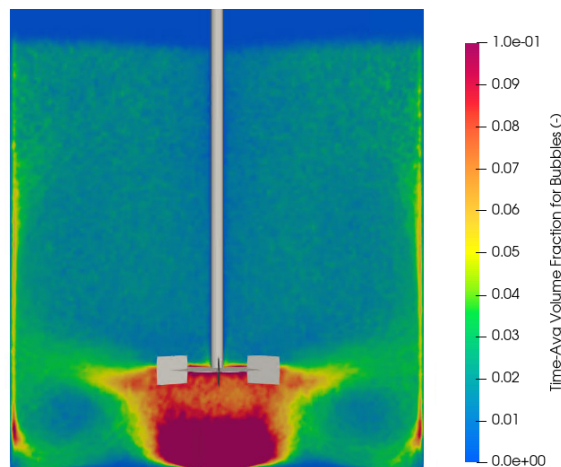


Figure 23: Contour plot of the gas fraction at an agitation speed of 385 rpm and GFR of  $0.00687 \text{ m}^3/s$ . The axis is scaled from 0-10% gas hold-up. The dark red spots indicate regions where the gas hold-up exceeds 10%.

A probable cause for the insufficient described dispersion of bubbles is the used drag correlation. Guan et al.[89] studied the effect of four drag models on the gas hold-up throughout the vessel when using an Eulerian-Eulerian approach on RANS simulations, and demonstrated that the used drag model is exceptionally important when predicting the gas-liquid flow inside vessels. In the simulations, they only considered the drag force and neglected all other relevant forces (which was suggested by Scargiali et al.[90]), and concluded that using DBS-Local and DBS-Global drag models give a good agreement with experimental data regarding the flow regimes, liquid flow field and gas hold-up. Furthermore, it was deduced that using the Schiller-Neumann drag correlation (Equation 5.1), a slight modification of the free particle model (Equation 3.28) described by Brown et al.[77], gives an overestimation of the gas hold-up near the impellers due

to an underestimation of the drag force. They also concluded that this drag model gives an underestimation of the gas hold-up with an increase in radial distance from the impeller.

$$C_{D0} = \begin{cases} \frac{24}{\text{Re}_b} (1 + 0.15 \text{Re}_b^{0.687}) & \text{Re} < 1000 \\ 0.44 & \text{Re} > 1000 \end{cases} \quad (5.1)$$

Zadghaffari et al.[91] simulated this particular case using different drag models with an Eulerian-Eulerian multiphase k- $\epsilon$  model, and compared the obtained gas hold-up with the experimentally obtained gas hold-up by Barigou et al.[31]. They concluded that the use of the Schiller-Neumann correlation resulted in a significant underprediction of the gas hold-up when compared with experimental data. However, when modifying the drag coefficient based on the force on a rising bubble in stagnant liquid (Equation 5.2) proposed by Scargiali et al.[90], they obtained results similar to the experiment. In this correlation, the terminal velocity of the bubble is the only significant contribution to the drag force.

$$C_D = \frac{V_p (\rho_g - \rho_l) g}{(1/2) A_p \rho_l U_T^2} \quad (5.2)$$

In this equation,  $U_T$  is the terminal velocity of bubbles in stagnant water. Zadghaffari et al. modified the terminal velocity correlation (Equation 5.4) by Mendelson et al.[92] by correlating it to the terminal velocity in an agitated tank,  $U_S$ :

$$\frac{U_S}{U_T} = 0.32 \tanh \left[ 19 \left( \frac{\eta}{d_b} \right) \left( \frac{\Delta \rho}{\rho_l} \right)^{0.5} - 1 \right] + 0.6 \quad (5.3)$$

$$U_T = \left[ \left( 2.14 \frac{\sigma}{\rho d} \right) + 0.505 g d \right]^{0.5} \quad (5.4)$$

In this correlation, the ratio  $\eta/d_b$  is the ratio between the Kolmogorov microscale ( $\eta = (\nu^3/\epsilon)^{0.25}$ ) and the bubble diameter. When using these correlations, Zadghaffari et. al were able to predict a gas hold-up which gave good agreement with the experimental results of Barigou and Greaves.

### 5.3 Velocity distribution in the impeller plane

Despite being outside of the scope of the current work, there is an interesting observation regarding the maximum velocity reached in the fluid worth mentioning. The maximum velocity at the impeller plane for an agitation speed of 385 RPM is shown in Figure 24. Despite the impeller rotating with a speed of 6.71 m/s, the CFD results reflect a maximum velocity of 13 m/s in the impeller wake. This same phenomenon is observed when the agitation rate is lowered too 180 RPM (3.14 m/s) where the maximum observed fluid velocity is 8.92 m/s. This was also observed in work done by Shu et al.[93] using the LBM with the highest velocity being 2.2 times larger than the impeller tip velocity. As this observation is outside the scope of the current study, this is left for further research.

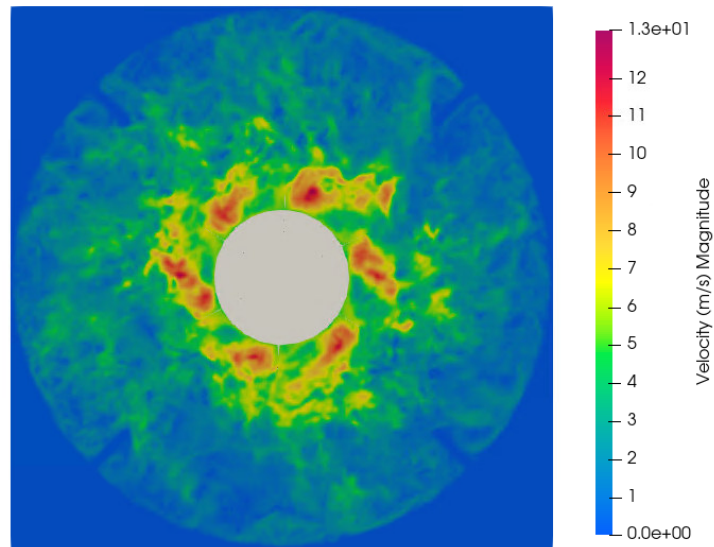


Figure 24: Contour plot of the fluid velocity at the impeller plane for an agitation rate of 385 rpm and a GFR of  $0.00687 \text{ m}^3/\text{s}$ . The axis is scaled from 0-13 m/s, with the red spots indicating areas reaching a velocity of 13 m/s.

## 6 Results - industrial fermentor

This chapter displays the obtained results of the industrial  $22m^3$  reactor of Stavanger, while at the same time discussing the results. The gas hold-up and power consumption of the (aerated) impellers are discussed. One case is compared to previously obtained CFD results using the Finite Volume CFD technique[26]. The experimental results are obtained from Vrabel et al.[24]. The source also contains unpublished results from Rob van der Lans.

### 6.1 Gas hold-up

The acquired gas hold-up using CFD and experiment is presented in Table 8. The gas hold-up, as before, underestimated compared to the experimental data set, which is especially prevalent for the lowest GFR of 2700 L/min. Interestingly, the dissimilarity between the CFD and experimental values for the gas hold-up diminishes as the GFR is increased, which can be observed in Figure 25a. The influence of the agitation speed on the gas hold-up can be observed in Figure 25b.

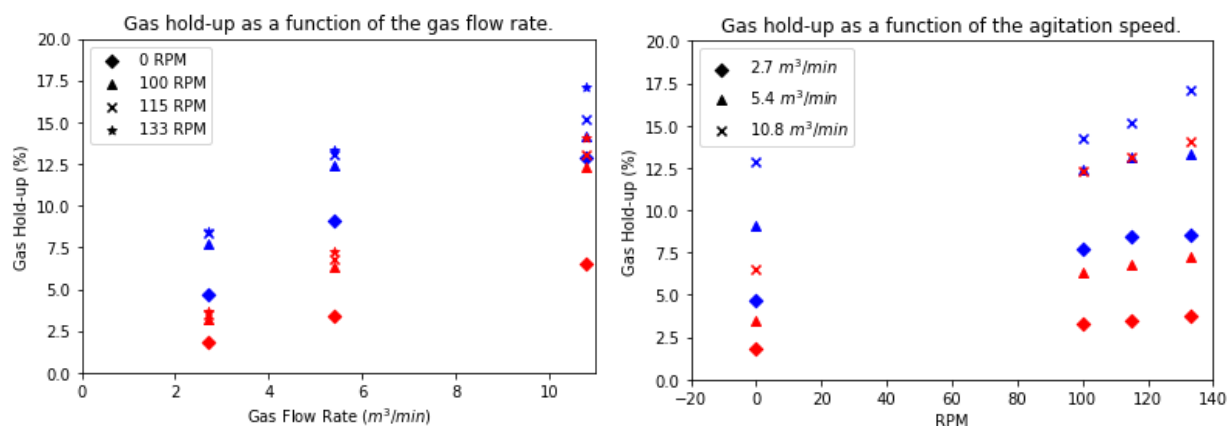
Table 8: Comparison of the LBM and experimental values for the gas hold-up.

(a) Gas Hold-up for the obtained CFD results and experimental results of the industrial fermentor.

	GFR (L/min)		
	2700	5400	10800
0	1.80%	3.44%	6.51%
100	3.26%	6.33%	12.34%
RPM 115	3.47%	6.78%	13.09%
133	3.71%	7.23%	14.06%

(b) Experimental results.

	GFR (L/min)		
	2700	5400	10800
0	4.7%	9.1%	12.9%
100	7.7%	12.4%	14.2%
RPM 115	8.4%	13.1%	15.2%
133	8.5%	13.3%	17.1%



(a) Gas hold-up for different agitation speeds as a function of the GFR.

(b) Gas hold-up for different GFR as a function of RPM.

Figure 25: Gas hold-up as a function of the RPM and the GFR. The blue color indicates experimental values, the red color indicates CFD values.

As discussed previously, the used drag correlation is insufficient to describe the dispersion and residence time of bubbles, leading to a lower gas hold-up in the vessels. It is therefore interesting that at the highest GFR the gas hold-up shows a significantly improved agreement with experimental data. A possibility for this increase in accuracy might be the overestimation

of the bubble swarm effect. As multiple bubbles are present in the system, the drag force will be influenced by the formed bubble swarms[94]. To account for bubble swarm effects, a correction needs to be added to the drag coefficient by relating it to the gas hold-up[95]:

$$C_{D_s} = C_D(1 - \alpha_g)^p \quad (6.1)$$

In which  $\alpha_g$  is the gas hold-up and  $p$  is the correction factor. In the current work, the drag coefficient was not related to the gas hold-up and swarm effects were thus not accounted for. This is because the used Free Particle model describes the drag on a single particle in a fluid, and thus therefore not account for the effect of multiple bubbles on the drag. By incorporating this correction into the model, the drag coefficient is lowered as the gas hold-up increases. This explains why at a lower superficial GFR, the gas hold-up deviates more significantly from the experimental data as the drag coefficient is underestimated. At the highest GFR, the under estimation of the drag coefficient is balanced with the over estimation regarding the bubble swarm effects, and thus the CFD results are more in line with experimental data. The Tomiyama drag correlation[96] could potentially lead to a better predicted gas holdup. This drag correlation has been commonly used for multiphase flows, and has proven to be an effective drag model to describe bubble dispersion throughout vessels[97][98]. Furthermore, this drag correlation has been utilized by Witz et al.[30] and Bernauer et al.[29] for large-scale reactors, in which the predicted gas hold-up showed good agreement with experimental data. They applied the Tomiyama drag coefficient for pure systems, as shown in Equation 6.2.

$$C_{D0} = \max \left\{ \min \left[ \frac{16}{Re_p} (1 + 0.15 Re_p^{0.687}), \frac{48}{Re_p} \right], \frac{8}{3} \frac{Eo}{Eo + 4} \right\} \quad (6.2)$$

in which  $Eo$  is the Eötvös number:

$$Eo = \frac{g(\rho_l - \rho_g)d_b^2}{\sigma} \quad (6.3)$$

## 6.2 Power consumption

The ungasged power consumption ( $P_o$ ) of the impellers are shown in Table 9. As expected, the resolved power dissipation is orders-of-magnitude lower compared to the power dissipation due to the unresolved eddies dissipating the bulk of the energy. There is a slight discrepancy between the observed power consumption of the impellers and the power dissipation. When the Power number is computed from the power consumption, the single impeller  $N_P \approx 3.6$ , which is an under prediction when compared to experimental data ( $N_P = 4.6-6.0$ [80]).

Table 9: CFD results for the ungasged power consumption.

RPM	Impeller 1 [W]	Impeller 2 [W]	Impeller 3 [W]	Impeller 4 [W]	Rotor [W]	Power Diss. [W]	Resolved Diss. [W]
100	2732.879	2829.699	2775.199	2647.509	13.6571	12024.67	108.26
115	4159.578	4332.023	4265.516	4042.246	20.9713	18320.24	143.5223
133	6406.005	6693.768	6622.277	6216.069	32.37857	28198.29	193.1378

The measured experimental power consumption is displayed in Table 10. When comparing the experimental power consumption with the computed power dissipation, there is a significant deviation. The most probable cause for the deviation is an under estimated EDR using a Smagorinsky coefficient of 0.1.

Table 10: Estimated power consumption of the experiment.

RPM	Power Consumption (W)
100	18700
115	29260
133	45100

The normalized EDR outline of the bottom impeller is plotted against the normalized tank radius as depicted in Figure 26. As with case 2, the computed EDR is too low compared to the experimental data of Ducci and Yianneskis[84]. When compared with the normalized EDR of case 2, it is observed that the maximum EDR for this current case is slightly lower.

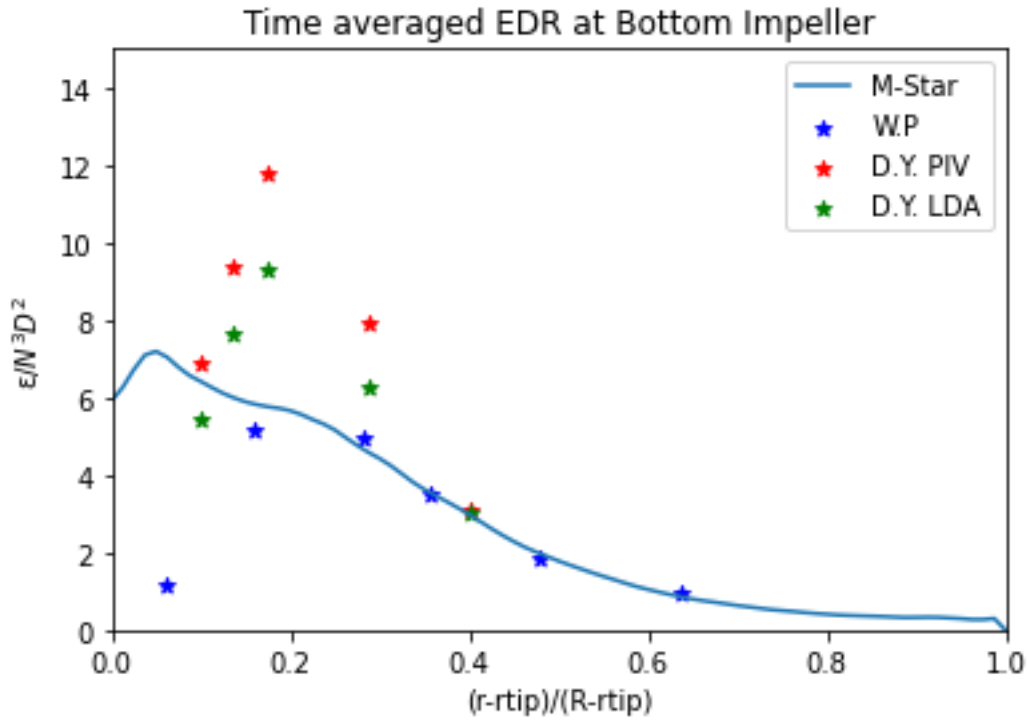


Figure 26: Plot of the normalized EDR. Abbreviations: W.P = Wu Patterson[83], D.Y = Ducci and Yianneskis[84].

The ratio of the power consumption at aeration ( $P_g$ ) with P are shown in Table 11. Where the experimental data indicates a significant reduction of power consumption when aerated, the CFD results lack those. At best, the power consumption when aerated has only dropped 3% for an agitation speed of 115 RPM and GFR of 5400 L/min, while the other cases predict a drop of 1 and 2%. The observed power reduction in the experimental set is due to the formation of gas cavities in the impeller wakes[99][100].

Table 11:  $P_g/P$  for different aeration rates and agitation speeds.

(a) CFD results.					(b) Experimental results.				
GFR (L/min)	RPM				GFR (L/min)	RPM			
		2700	5400	10800			2700	5400	10800
100.2		0.98	0.99	0.99	100.2		0.50	-	0.33
115		0.98	0.97	0.98	115		0.55	-	0.34
133		0.98	0.98	0.98	133		0.56	-	0.37

Figure 27a displays the velocity contour at the impeller plane which is the second from bottom impeller. The red spots indicate trailing vortices behind the impeller blades, which have the highest velocity. While comparing this with the gas hold-up in Figure 27b, there seems to be no formation of gas cavities residing in the trailing vortices.

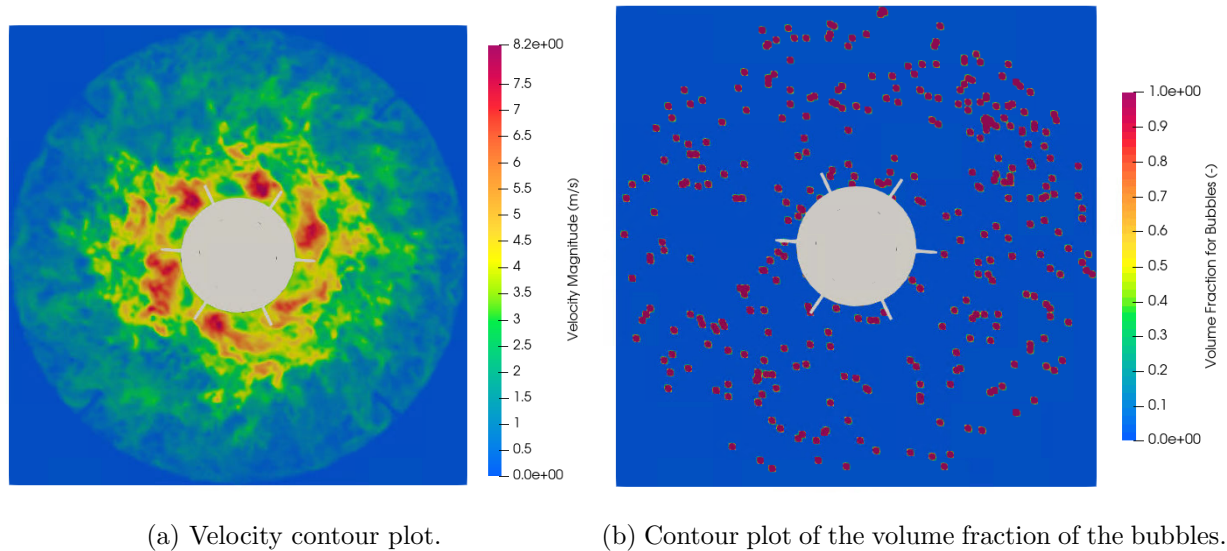


Figure 27: Velocity and bubble volume fraction contour plot at the impeller plane.

The Euler-Lagrangian approach of modelling the bubble particles could have implications for the formation of gas cavities in the trailing vortices. In the current approach, the Lagrangian bubbles inform the Eulerian flow field via two-way coupling using Newton's third law. Via this coupling, the sum of the gravity, buoyancy, virtual mass and the drag forces acting on the bubble are applied in reverse on the fluid voxel. Via DNS, Oweis et al.[101] indicated how the pressure gradient arising from vortices attracts small (non-condensable) gas bubble which leads to a significant increase of gas concentration in said cavities. As the pressure gradient was not applied in the current work, this will negatively influence the attraction of small bubbles to the trailing vortices. Cheng et al.[102] also showed how the pressure gradient significantly increases the gas concentration at the vortices. Furthermore, they argued that the current Lagrangian bubble tracking is insufficient to describe the formation of gas cavities inside the flow field. They proposed a cavitation model where the the total bubble pressure, vapor pressure and partial pressure of non-condensable gas is redirected to the solver to simulate gas cavities in the Eulerian flow field.

The fluid density contour and fluid volume fraction contour at the same impeller plane as before are shown in Figure 28. The bubble particles ensure a decrease of fluid density, however it does not inform a difference in the fluid volume fraction, which is unity throughout the impeller plane while there are bubble volumes present, as depicted in Figure 27b. With the proposed model of Cheng et al. the fluid volume would be affected by the presence of gas cavities in the Eulerian flow field.

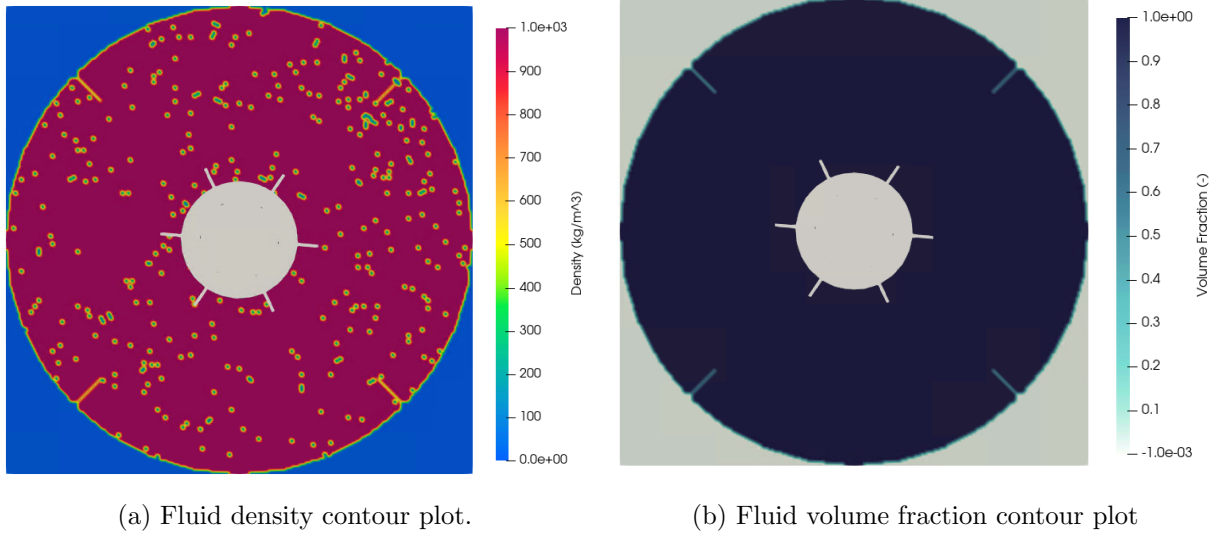


Figure 28: Contour plots of the density and volume fraction of the liquid at the impeller plane.

In addition, the setting of the bubble removal fraction described in subsection 4.3.1 could influence the formation of cavities. By setting this value to 0.1, representing the liquid fraction, ensured that bubbles left the tank when in contact with the free surface. However, as gas cavities are essentially formed by agglomerations of bubbles, it could have an impact on the removal of bubbles in the trailing vortices if gas cavities are formed. In the software update of M-star there is a Lagrange-to-Euler conversion, where agglomerations of bubbles are converted into empty lattice nodes to model the formation of gas cavities, which is essentially the proposal of Cheng et al.[102].

### 6.3 Comparison CFD techniques

The case with an agitation rate of 180 RPM and GFR of 10820 L/min was also performed by Haringa et al.[26], using a Finite Volume CFD with the  $k-\epsilon$  RANS approach, and is therefore compared to the LBM and experimental values. Table 12 show the values of the experimentally determined gas hold-up, power number. The mean bubble diameter, in addition to the previous mentioned parameters, also shown for both CFD approaches. As mentioned earlier, there is an under prediction of the gas hold-up when using the current LBM set-up, which is due to incorrect modelling of the drag force on the bubble. Experimental data regarding the mean bubble size is lacking, and as such the mean bubble size ( $d_{10}$ ) of the current work can only be compared to the obtained mean Sauter bubble size ( $d_{32}$ ) obtained by Haringa et al. They mentioned that the mean bubble size of 8.9 mm is an overestimation of the size when compared to lab scale studies of Barigou and Greaves[31]. When comparing the obtained mean  $d_{10}$  bubble size using the LBM, it is a severe underestimation compared to Haringa et al.

Table 12: Comparison of the obtained results for LB-CFD, FV-CFD[26] and experimental results.

	CFD LB	CFD FV	Exp
Gas Hold-up (%)	14.06	17.6	17.1
$N_P$ (gassed)	15.3	9.6	9.2
$d_b(mm)$	0.45	8.9	-

The displayed  $N_P$  reflects the combined power number of all the present impellers, and is significantly higher compared with the FV-CFD approach and experimental values. This is

due to the absence of gas cavities present in the vortex trails, and the non-dependency of the gas hold-up on the consumed power in the current set-up. It is worth noting that the power number of the impellers fluctuate significantly under aerated conditions. This is reflected in Figure 29, where the power number is plotted as a function of time. The most probable reason for this fluctuation is that the numerical algorithm matches the power number with the power dissipation as the density of the fluid changes due to the present bubbles.

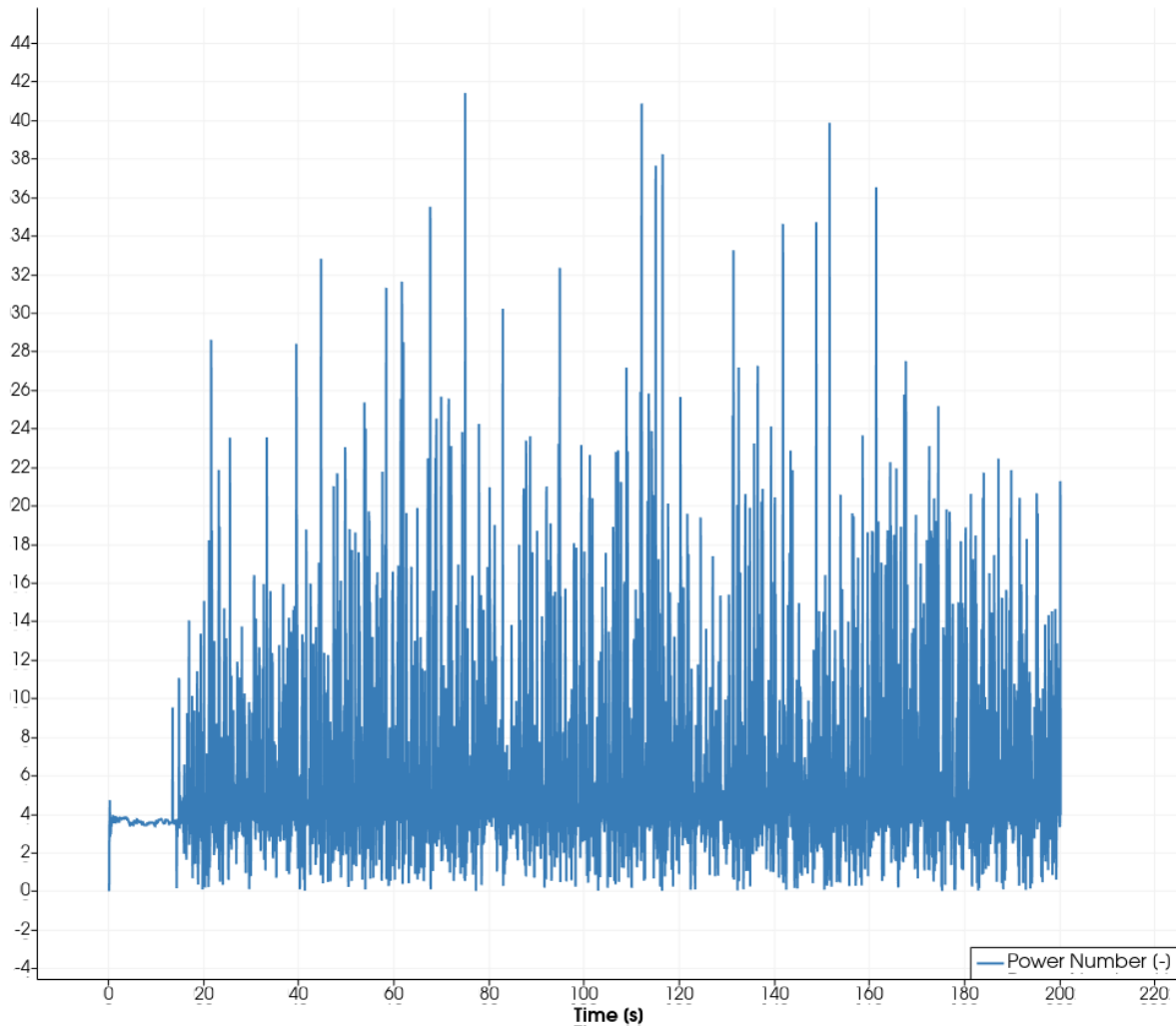


Figure 29: Power number of the impeller as a function of time.

A comparison between both CFD approaches regarding the gas hold-up is shown in Figure 30. Both axis are scaled from 0-100%, while it is noted that the color schemes vary for both cases. The multiple Rushton turbines lead to clear compartmentalization for both approaches. However, the approach used by Haringa et al. leads to a superior dispersion of the gas fraction throughout the vessel, which is especially prevalent for the gas hold-up above the top impeller. They used Fluent’s Universal drag model<sup>9</sup>, which is established from the drag model of Ishii et al.[103], which highlights the importance of a correctly modelled drag force.

<sup>9</sup>(2009) Ansys Fluent 12.0 Theory guide - 16.5.4 Interphase Exchange Coefficients. Ansys, Inc. Retrieved January 10, 2023, from <https://www.afs.enea.it/project/neptunius/docs/fluent/html/th/node323.htm>

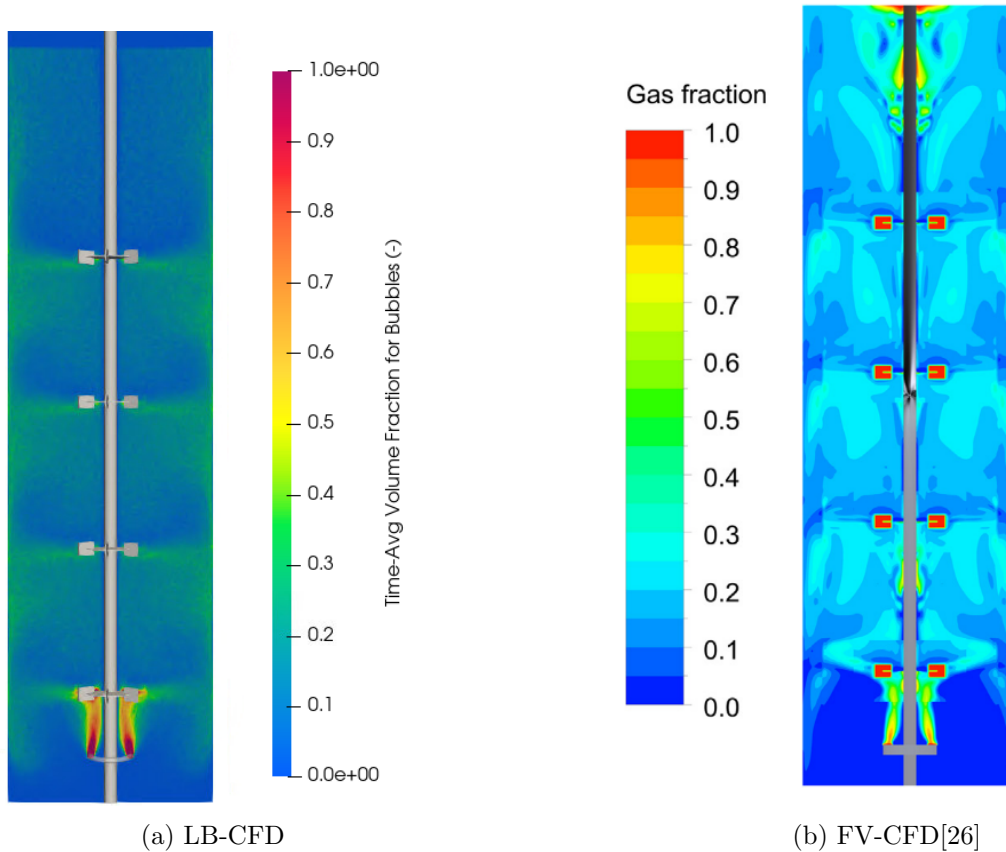


Figure 30: Comparison of the gas hold-up between the LB-CFD and FV-CFD for an agitation rate of 133 rpm and gas flow rate of 10820 L/min. Both axis are scaled from 0-100%, although the color schemes are different.

As mentioned the obtained mean  $d_{10}$  is very low compared to the mean  $d_{32}$  using FV-CFD. The histogram in Figure 31 illustrates the amount of parcels present in the system with their corresponding equilibrium diameter. It is observed that the bulk of the parcels have an equilibrium diameter between 4.5-5 mm. As the number scale ensures the conservation of mass as the equilibrium diameter evolves, the amount of fictitious bubbles present in the parcels with a low diameter are considerably higher than the amount of bubbles represented by the parcel with a large diameter. This implicates that parcels with a small equilibrium diameter represent a higher amount of bubbles, and as such the  $d_{10}$  is skewed to a lower mean diameter.

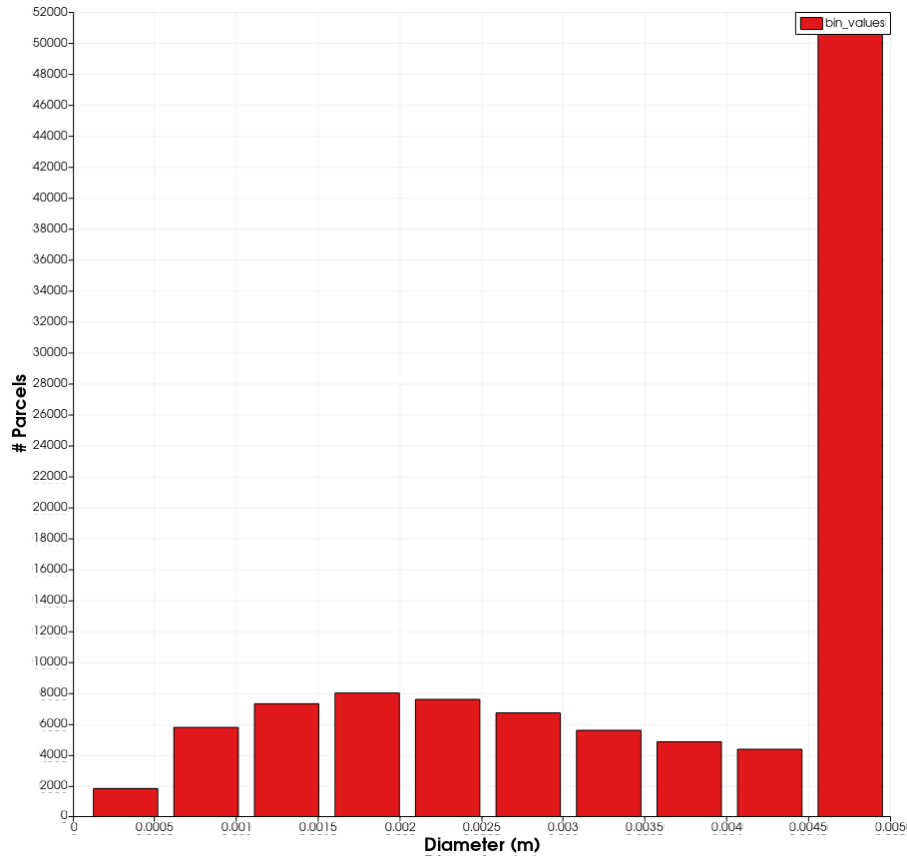


Figure 31: Parcel size histogram for a maximum coalescence diameter of 5mm.

As an enforced maximum coalescence diameter of 5 mm leads to a disproportionate amount of parcels with an equilibrium diameter between 4.5-5mm, another simulation was conducted where the maximum coalescence diameter was 2.5cm. The corresponding histogram is depicted in Figure 32. The bulk of the parcels have an equilibrium diameter below 5 mm but nevertheless, a significant amount of particles have a higher corresponding diameter. An enforced maximum coalescence diameter has a negligible effect on the gas hold-up (14.06%) and mean  $d_{10}$  (0.46 mm). The corresponding mean  $d_{43}$  is 3.6 mm, and seems more reasonable to use when comparing the mean bubble size with the mean  $d_{32}$  obtained by Haringa et al.[26].

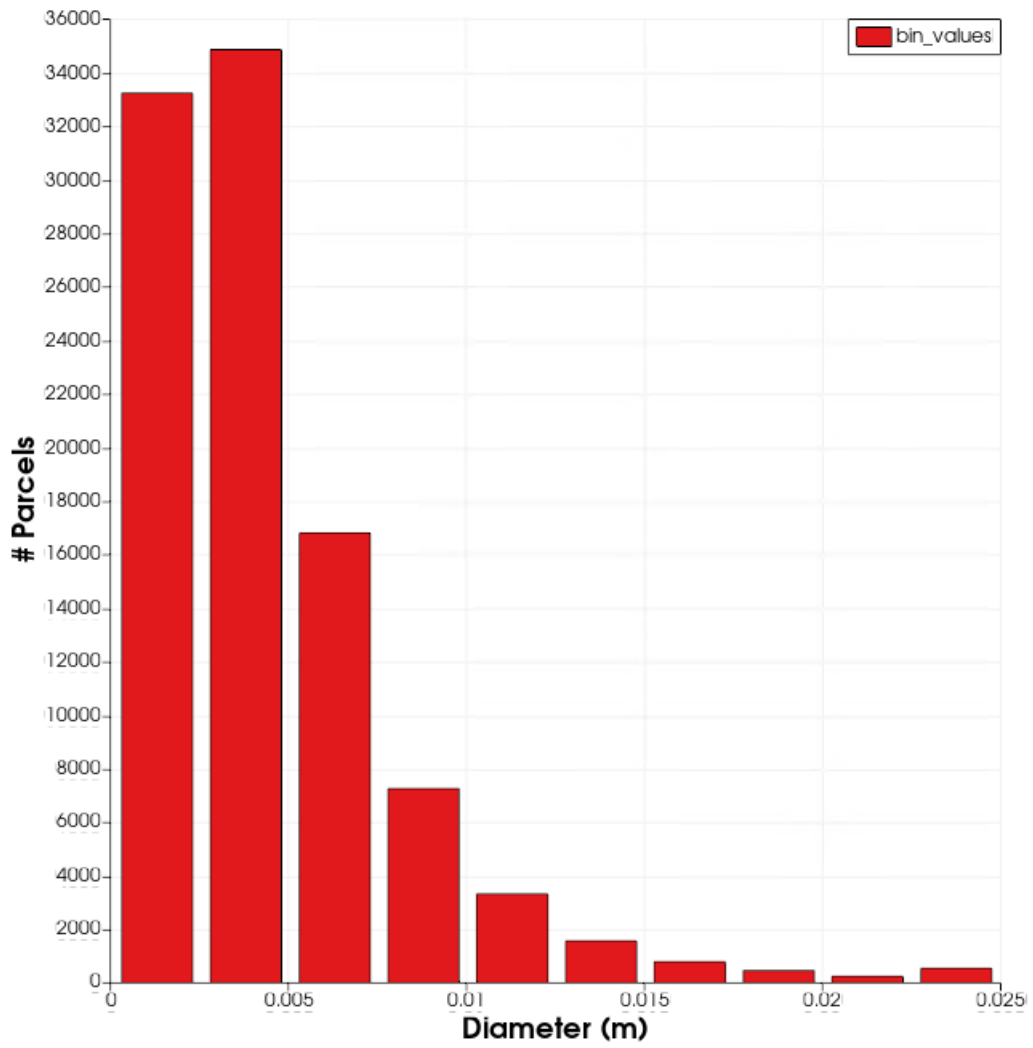


Figure 32: Parcel Size histogram for a maximum coalescence diameter of 2.5 cm.

---

## 7 Conclusion and Recommendations

In the present work, the LBM CFD approach was used to model three bench mark cases. This was done by using the models provided with M-star simulations (M-Star Simulations, LLC) and comparing this to the results obtained by Thomas et al.[32] to verify the set-up. The conclusions from this analysis provided a way to use the LBM to simulate a small vessel and acquire the BSD and gas hold-up to compare the results with experimental data of Barigou et al.[31]. The third case was the simulation of an industrial-scaled reactor located in Stavanger, comparing the obtained gas hold-up and power consumption with data from Vrabel et al.[24].

The conducted simulations used the LES turbulence model to resolve the turbulent fluid flow, and Euler-Lagrangian tracking of the bubbles using the parcel approach. These parcels moved throughout the vessel according to Newton's second law, experiencing the effects of the virtual mass force, drag force, buoyancy and gravity. These settings were verified by comparing the gas hold-up, bubble diameter and amount of bubbles present in the system with the obtained results of Thomas et al.[32], and were used for the succeeding cases.

The Free Particle drag model is not suitable to describe the drag force acting on the bubbles, as the gas hold-up was significantly underestimated for both this case and the industrial-scaled tank. However, an increase of GFR led to better agreement with experimental data. This is probably due to the omission of the bubble swarm effect, counterbalancing the insufficiently described drag correlation.

When comparing the BSD with the experimentally obtained results of Barigou et al. it was found that setting the maximum coalescence diameter to 1 cm leads to an over estimation of the bubble sizes at the top of the vessel. Using the parcel model implied that the bubble size evolved as a function of the EDR, implicitly capturing break-up and coalescence events. By modelling the smallest eddies by setting a Smagorinsky coefficient of 0.1, the EDR was underestimated, resulting in too large bubbles at the top of the vessel. Setting the maximum coalescence diameter to 5 mm resulted in a BSD which was more agreeable with experimental data, although the predicted gas hold-up did not improve significantly. Using the discrete approach should lead to a better bubble size distribution throughout the vessel, as this approach explicitly models bubble break-up and coalescence. However as the parcel approach was valid for the case studies, it is not expected that the discrete approach would lead to superior agreement with experimental data regarding the gas hold-up.

The Euler-Lagrangian way of modelling bubble particles did not lead to the formation of gas cavities in the trailing vortices generated by the impeller, which in turn did not lead to a drop in power consumption when the tank was aerated. The most probable causes for the absence of gas cavity formation is the used approach of modeling bubbles, while also neglecting the pressure gradient.

### 7.1 Recommendations

Due to time constraints, the implementation of different drag models and the effect of applying the pressure gradient was not tested. It is recommended to implement varying drag correlations, such as the Tomiyama drag correlation, which has proven to show adequate predictions for the gas hold-up for industrial-sized reactors by Witz et al.[30] and Bernauer et al.[29]. Zadghaffari et al.[91] used a modified drag coefficient based on a rising bubble in stagnant liquid. With this drag correlation, they were capable of predicting a gas hold-up which was in good agreement with the data of Barigou and Greaves. It would therefore be beneficial to implement this drag correlation and verify whether this correlation can be suitable for the currently used parcel

---

approach, as it will probably be unfeasible, if not impossible, to use the discrete approach for industrial-scaled reactors with high gas flow rate. Other drag correlations which could be implemented are the DBS-local and DBS-Global proposed by Guan et al.[89]. Setting the maximum coalescence to 5 mm leads to reasonable agreement of the BSD with experimental, but setting the Smagorinsky coefficient to 0.2 could potentially lead to an EDR which will lead to a better capturing of the EDR in the impeller outflow, resulting in a better captured BSD throughout the vessel when using the parcel approach.

It is also recommended to test the new update of M-star, which allows for the Lagrangian-to-Euler conversion of bubbles into empty lattice nodes. This method is also recommended by Cheng et al.[102], and could lead to the formation of gas cavities in the impeller trailing vortices. Using this, a more accurate description of power reduction under aeration could potentially be observed.

Lastly, it is recommended to further test the applicability of the LBM for industrial-scaled reactors. As experimental data is scarce for such reactors, it is of necessity to fully exploit the available data for the current bioreactor by Vrabel et al.[24] and Larsson et al.[25].

---

## Bibliography

- [1] Luca Riccardo Formenti, Anders Nørregaard, Andrijana Bolic, Daniela Quintanilla Hernandez, Timo Hagemann, Anna-Lena Heins, Hilde Larsson, Lisa Mears, Miguel Mauricio-Iglesias, Ulrich Kruehne, et al. Challenges in industrial fermentation technology research. *Biotechnology journal*, 9(6):727–738, 2014.
- [2] Ólafur Ögmundarson, Sumesh Sukumara, Markus J Herrgård, and Peter Fantke. Combining environmental and economic performance for bioprocess optimization. *Trends in Biotechnology*, 38(11):1203–1214, 2020.
- [3] Fernando N Santos-Navarro, Yadira Boada, Alejandro Vignoni, and Jesús Picó. Gene expression space shapes the bioprocess trade-offs among titer, yield and productivity. *Applied Sciences*, 11(13):5859, 2021.
- [4] Ronald A Rader and Eric S Langer. Biopharmaceutical manufacturing: Historical and future trends in titers, yields, and efficiency in commercial-scale bioprocessing. *BioProcessing Journal*, 13(4), 2014.
- [5] F Bezzo, S Macchietto, and CC Pantelides. General hybrid multizonal/cfd approach for bioreactor modeling. *AIChE Journal*, 49(8):2133–2148, 2003.
- [6] Henk Noorman. An industrial perspective on bioreactor scale-down: what we can learn from combined large-scale bioprocess and model fluid studies. *Biotechnology journal*, 6(8):934–943, 2011.
- [7] Felix Garcia-Ochoa and Emilio Gomez. Bioreactor scale-up and oxygen transfer rate in microbial processes: an overview. *Biotechnology advances*, 27(2):153–176, 2009.
- [8] CJ Brouckaert, GA Ekama, BM Brouckaert, and DS Ikumi. Integration of complete elemental mass-balanced stoichiometry and aqueous-phase chemistry for bioprocess modelling of liquid and solid waste treatment systems- part 2: Bioprocess stoichiometry. *Water SA*, 47(3):289–308, 2021.
- [9] Michael J Prince and Harvey W Blanch. Bubble coalescence and break-up in air-sparged bubble columns. *AIChE journal*, 36(10):1485–1499, 1990.
- [10] Kenji Tabata and Ichiro Okura. Hydrogen and methanol formation utilizing bioprocesses. *Journal of the Japan Petroleum Institute*, 51(5):255–263, 2008.
- [11] Peng Hu, Sagar Chakraborty, Amit Kumar, Benjamin Woolston, Hongjuan Liu, David Emerson, and Gregory Stephanopoulos. Integrated bioprocess for conversion of gaseous substrates to liquids. *Proceedings of the National Academy of Sciences*, 113(14):3773–3778, 2016.
- [12] Y Kawase and M Moo-Young. Mathematical models for design of bioreactors: Applications of: Kolmogoroff’s theory of isotropic turbulence. *The Chemical Engineering Journal*, 43(1):B19–B41, 1990.
- [13] Gianni Donati and Renato Paludetto. Scale up of chemical reactors. *Catalysis today*, 34(3):483–534, 1997.
- [14] S Hernandez, Lilibeth Niño, and G Gelves. Simulating of microbial growth scale up in a stirred tank bioreactor for aerobic processes using computational fluid dynamics. In *Journal of Physics: Conference Series*, volume 1655, page 012109. IOP Publishing, 2020.

- 
- [15] Chung-Hur Lee, LE Erickson, and LA Glasgow. Bubble breakup and coalescence in turbulent gas-liquid dispersions. *Chemical Engineering Communications*, 59(1-6):65–84, 1987.
- [16] Michael J Prince and Harvey W Blanch. Bubble coalescence and break-up in air-sparged bubble columns. *AIChE journal*, 36(10):1485–1499, 1990.
- [17] Mattia Polli, Marco Di Stanislao, Roberto Bagatin, Eiman Abu Bakr, and Maurizio Masi. Bubble size distribution in the sparger region of bubble columns. *chemical Engineering science*, 57(1):197–205, 2002.
- [18] Roland Rzehak and Eckhard Krepper. Cfd modeling of bubble-induced turbulence. *International Journal of Multiphase Flow*, 55:138–155, 2013.
- [19] Guan Wang, Cees Haringa, Henk Noorman, Ju Chu, and Yingping Zhuang. Developing a computational framework to advance bioprocess scale-up. *Trends in biotechnology*, 38(8):846–856, 2020.
- [20] Shuli Shu, Jingchang Zhang, and Ning Yang. Gpu-accelerated transient lattice boltzmann simulation of bubble column reactors. *Chemical Engineering Science*, 214:115436, 2020.
- [21] Hooman Yadollahi Farsani, Johannes Wutz, Brian DeVincentis, John A Thomas, and Seyed Pouria Motevalian. Modeling mass transfer in stirred microbioreactors. *Chemical Engineering Science*, 248:117146, 2022.
- [22] Alankar Agarwal, Gurveer Singh, and Akshay Prakash. Effect of baffles on the flow hydrodynamics of dual-rushton turbine stirred tank bioreactor—a cfd study. *Brazilian Journal of Chemical Engineering*, 38(4):849–863, 2021.
- [23] R Robert Nourgaliev, Truc-Nam Dinh, Theo G Theofanous, and D Joseph. The lattice boltzmann equation method: theoretical interpretation, numerics and implications. *International Journal of Multiphase Flow*, 29(1):117–169, 2003.
- [24] Peter Vrabel, Rob GJM van der Lans, Karel Ch AM Luyben, Lotte Boon, and Alvin W Nienow. Mixing in large-scale vessels stirred with multiple radial or radial and axial up-pumping impellers: modelling and measurements. *Chemical Engineering Science*, 55(23):5881–5896, 2000.
- [25] G Larsson, M Törnkvist, E Ståhl Wernersson, Ch Trägårdh, H Noorman, and S-O Enfors. Substrate gradients in bioreactors: origin and consequences. *Bioprocess Engineering*, 14(6):281–289, 1996.
- [26] Cees Haringa, Amit T Deshmukh, Robert F Mudde, and Henk J Noorman. Euler-lagrange analysis towards representative down-scaling of a 22 m<sup>3</sup> aerobic s. cerevisiae fermentation. *Chemical Engineering Science*, 170:653–669, 2017.
- [27] Maike Kuschel, Jürgen Fitschen, Marko Hoffmann, Alexandra von Kameke, Michael Schlüter, and Thomas Wucherpfennig. Validation of novel lattice boltzmann large eddy simulations (lb les) for equipment characterization in biopharma. *Processes*, 9(6):950, 2021.
- [28] Harry E A van den Akker. Lattice Boltzmann Modeling for Chemical Engineering (Volume 55). 55:1–12, 2020.
- [29] Sören Bernauer, Philipp Eibl, Christian Witz, Johannes Khinast, and Timo Hardiman. Analyzing the effect of using axial impellers in large-scale bioreactors. *Biotechnology and Bioengineering*, 119(9):2494–2504, 2022.

- 
- [30] Christian Witz, Daniel Treffer, Timo Hardiman, and Johannes Khinast. Local gas holdup simulation and validation of industrial-scale aerated bioreactors. *Chemical Engineering Science*, 152:636–648, 2016.
- [31] Mostafa Barigou and Malcolm Greaves. Bubble-size distributions in a mechanically agitated gas—liquid contactor. *Chemical Engineering Science*, 47(8):2009–2025, 1992.
- [32] John A Thomas, Brian DeVincentis, Navraj Hanspal, and Richard O Kehn. Predicting gas-liquid mass transfer rates in reactors using a bubble parcel model. *Chemical Engineering Science*, page 118183, 2022.
- [33] Peter Alan Davidson. *Turbulence: an introduction for scientists and engineers*. Oxford university press, 2015.
- [34] Y Kawase and M Moo-Young. Mixing time in bioreactors. *Journal of Chemical Technology & Biotechnology*, 44(1):63–75, 1989.
- [35] Andrey Nikolaevich Kolmogorov. The local structure of turbulence in incompressible viscous fluid for very large reynolds numbers. *Cr Acad. Sci. URSS*, 30:301–305, 1941.
- [36] H Belmabrouk and M Michard. Taylor length scale measurement by laser doppler velocimetry. *Experiments in Fluids*, 25(1):69–76, 1998.
- [37] Hendrik Tennekes, John Leask Lumley, Jonh L Lumley, et al. *A first course in turbulence*. MIT press, 1972.
- [38] Arif Hossain. *Design of a High Intensity Turbulent Combustion System*. PhD thesis, 05 2015.
- [39] Mike Mollet, Ningning Ma, Yang Zhao, Robert Brodkey, Ron Taticcek, and Jeffrey J Chalmers. Bioprocess equipment: characterization of energy dissipation rate and its potential to damage cells. *Biotechnology progress*, 20(5):1437–1448, 2004.
- [40] Diego Mesa and Pablo R Brito-Parada. Bubble size distribution in aerated stirred tanks: Quantifying the effect of impeller-stator design. *Chemical Engineering Research and Design*, 160:356–369, 2020.
- [41] Przemyslaw B Kowalczyk and Jan Drzymala. Physical meaning of the sauter mean diameter of spherical particulate matter. *Particulate Science and Technology*, 34(6):645–647, 2016.
- [42] Julius O Hinze. Fundamentals of the hydrodynamic mechanism of splitting in dispersion processes. *AIChE journal*, 1(3):289–295, 1955.
- [43] RD Kirkpatrick and MJ Lockett. The influence of approach velocity on bubble coalescence. *Chemical Engineering Science*, 29(12):2363–2373, 1974.
- [44] Boris Boshenyatov. Laws of bubble coalescence and their modeling. *Journal of Magneto-hydrodynamics and Plasma Research*, 18(4):311, 2013.
- [45] J Sauter. Determining size of drops in fuel mixture of internal combustion engines. Technical report, 1926.
- [46] Somesh Mishra, Vikash Kumar, Jayati Sarkar, and Anurag S Rathore. Cfd based mass transfer modeling of a single use bioreactor for production of monoclonal antibody bio-therapeutics. *Chemical Engineering Journal*, 412:128592, 2021.

- 
- [47] Henrique JO Pinho, Dina MR Mateus, and Sebastião S Alves. Computation of bubble mean diameters using probability distribution functions. In *AIP Conference Proceedings*, volume 1906, page 110008. AIP Publishing LLC, 2017.
- [48] Alessandro Paglianti. Simple model to evaluate loading/flooding transition in aerated vessels stirred by rushton disc turbines. *The Canadian Journal of Chemical Engineering*, 80(4):1–5, 2002.
- [49] K Van’t Riet and John M Smith. The trailing vortex system produced by rushton turbine agitators. *Chemical Engineering Science*, 30(9):1093–1105, 1975.
- [50] V Hudcova, V Machon, and AW Nienow. Gas–liquid dispersion with dual rushton impellers. *Biotechnology and Bioengineering*, 34(5):617–628, 1989.
- [51] MMCG Warmoeskerken and John M Smith. The flooding transition with gassed rushton turbines. In *Fluid Mixing II: A Symposium Organised by the Yorkshire Branch and the Fluid Mixing Processes Subject Group of the Institution of Chemical Engineers and Held at Bradford University, 3-5 April 1984*, number 89, page 59. Elsevier, 2013.
- [52] Alvin W Nienow and David Miles. Impeller power numbers in closed vessels. *Industrial & Engineering Chemistry Process Design and Development*, 10(1):41–43, 1971.
- [53] Mahsa Taghavi, Ramin Zadghaffari, Jafarsadegh Moghaddas, and Yousef Moghaddas. Experimental and cfd investigation of power consumption in a dual rushton turbine stirred tank. *Chemical Engineering Research and Design*, 89(3):280–290, 2011.
- [54] WALDEMAR Bujalski, AW Nienow, S Chatwin, and M Cooke. The dependency on scale of power numbers of rushton disc turbines. *Chemical Engineering Science*, 42(2):317–326, 1987.
- [55] D Chapple, SM Kresta, A Wall, and A Afacan. The effect of impeller and tank geometry on power number for a pitched blade turbine. *Chemical Engineering Research and Design*, 80(4):364–372, 2002.
- [56] Francesco Maluta, Alessandro Paglianti, and Giuseppina Montante. Two-fluids rans predictions of gas cavities, power consumption, mixing time and oxygen transfer rate in an aerated fermenter scale-down stirred with multiple impellers. *Biochemical Engineering Journal*, 166:107867, 2021.
- [57] Fumio Saito, Alvin W Nienow, Sidney Chatwin, and Iain PT Moore. Power, gas dispersion and homogenisation characteristics of scaba srgt and rushton turbine impellers. *Journal of chemical engineering of Japan*, 25(3):281–287, 1992.
- [58] Timm Krüger, Halim Kusumaatmaja, Alexandr Kuzmin, Orest Shardt, Goncalo Silva, and Erlend Magnus Viggen. *The lattice Boltzmann method*. Graduate Texts in Physics. Springer International Publishing, 2017.
- [59] Gregory Nicholas De Boer, Adam Johns, Nicolas Delbosc, Daniel Burdett, Morgan Tatchell-Evans, Jonathan Summers, and Remi Baudot. Three computational methods for analysing thermal airflow distributions in the cooling of data centres. *International Journal of Numerical Methods for Heat & Fluid Flow*, 2018.
- [60] Xiaoyi He and Gary D Doolen. Thermodynamic foundations of kinetic theory and lattice boltzmann models for multiphase flows. *Journal of Statistical Physics*, 107(1):309–328, 2002.

- 
- [61] Alessandro De Rosis and Christophe Coreixas. Multiphysics flow simulations using d3q19 lattice boltzmann methods based on central moments. *Physics of Fluids*, 32(11):117101, 2020.
- [62] Prabhu Lal Bhatnagar, Eugene P Gross, and Max Krook. A model for collision processes in gases. i. small amplitude processes in charged and neutral one-component systems. *Physical review*, 94(3):511, 1954.
- [63] Philipp Neumann, Hans-Joachim Bungartz, Miriam Mehl, Tobias Neckel, and Tobias Weinzierl. A coupled approach for fluid dynamic problems using the pde framework peano. *Communications in Computational Physics*, 12(1):65–84, 2012.
- [64] Sydney Chapman and Thomas George Cowling. *The mathematical theory of non-uniform gases: an account of the kinetic theory of viscosity, thermal conduction and diffusion in gases*. Cambridge university press, 1990.
- [65] Jun Li. Chapman-enskog expansion in the lattice boltzmann method. *arXiv preprint arXiv:1512.02599*, 2015.
- [66] Jacqueline H Chen. Petascale direct numerical simulation of turbulent combustion—fundamental insights towards predictive models. *Proceedings of the Combustion Institute*, 33(1):99–123, 2011.
- [67] Khelifa Hami. Turbulence modeling a review for different used methods. *International Journal of Heat and Technology*, 39(1):227–234, 2021.
- [68] BT Kannan, S Karthikeyan, and Senthilkumar Sundararaj. Comparison of turbulence models in simulating axisymmetric jet flow. In *Innovative Design and Development Practices in Aerospace and Automotive Engineering*, pages 401–407. Springer, 2017.
- [69] Stefan Heinz. A review of hybrid rans-les methods for turbulent flows: Concepts and applications. *Progress in Aerospace Sciences*, 114:100597, 2020.
- [70] Sal Rodriguez. *Applied computational fluid dynamics and turbulence modeling*. Springer, 2019.
- [71] Hampus Tober and Erik Hänninger. Evaluation of openfoam performance for rans simulationsof flow around a naca 4412 airfoil, 2018.
- [72] Franck Nicoud. Unsteady flows modeling and computation. *LECTURE SERIES-VON KARMAN INSTITUTE FOR FLUID DYNAMICS*, 9:3, 2007.
- [73] JJJ Gillissen and HEA Van den Akker. Direct numerical simulation of the turbulent flow in a baffled tank driven by a rushton turbine. *AIChE Journal*, 58(12):3878–3890, 2012.
- [74] Christoph Rettinger and Ulrich Rüde. A coupled lattice boltzmann method and discrete element method for discrete particle simulations of particulate flows. *Computers & Fluids*, 172:706–719, 2018.
- [75] Nikolay Ivanov Kolev. Drag, lift, and virtual mass forces. In *Multiphase flow dynamics 2*, pages 31–85. Springer, 2011.
- [76] GI Kelbaliyev. Drag coefficients of variously shaped solid particles, drops, and bubbles. *Theoretical Foundations of Chemical Engineering*, 45(3):248–266, 2011.
- [77] Phillip P Brown and Desmond F Lawler. Sphere drag and settling velocity revisited. *Journal of environmental engineering*, 129(3):222–231, 2003.

- 
- [78] Liang Wen Rong, Kejun J Dong, and AB Yu. Lattice-boltzmann simulation of fluid flow through packed beds of uniform spheres: Effect of porosity. *Chemical Engineering Science*, 99:44–58, 2013.
- [79] Franck Nicoud and Frédéric Ducros. Subgrid-scale stress modelling based on the square of the velocity gradient tensor. *Flow, turbulence and Combustion*, 62(3):183–200, 1999.
- [80] Cees Haringa. An analysis of organism lifelines in an industrial bioreactor using lattice-boltzmann cfd. *Engineering in Life Sciences*, 23(1):e2100159, 2022.
- [81] Li Zheng and Poojitha D Yapa. Buoyant velocity of spherical and nonspherical bubbles/-droplets. *Journal of Hydraulic Engineering*, 126(11):852–854, 2000.
- [82] Ivo Roghair, H Kuipers, et al. Drag force on bubbles in bubble swarms. In *Seventh International Conference on CFD in the Minerals and Process Industries CSIRO, Melbourne, Australia 9-11 December 2009*, 2009.
- [83] H Wu and GK Patterson. Laser-doppler measurements of turbulent-flow parameters in a stirred mixer. *Chemical engineering science*, 44(10):2207–2221, 1989.
- [84] A Ducci and M Yianneskis. Direct determination of energy dissipation in stirred vessels with two-point lda. *AIChE journal*, 51(8):2133–2149, 2005.
- [85] H Hartmann, JJ Derksen, C Montavon, J Pearson, IS Hamill, and HEA Van den Akker. Assessment of large eddy and rans stirred tank simulations by means of lda. *Chemical Engineering Science*, 59(12):2419–2432, 2004.
- [86] Jos Derksen and Harry EA Van den Akker. Large eddy simulations on the flow driven by a rushton turbine. *AIChE Journal*, 45(2):209–221, 1999.
- [87] Angélique Delafosse, Alain Line, Jerome Morchain, and Pascal Guiraud. Les and urans simulations of hydrodynamics in mixing tank: comparison to piv experiments. *Chemical Engineering Research and Design*, 86(12):1322–1330, 2008.
- [88] Miroslav Soos, René Kaufmann, Raphael Winteler, Martin Kroupa, and Beat Lüthi. Determination of maximum turbulent energy dissipation rate generated by a rushton impeller through large eddy simulation. *AIChE Journal*, 59(10):3642–3658, 2013.
- [89] Xiaoping Guan, Xinju Li, Ning Yang, and Mingyan Liu. Cfd simulation of gas-liquid flow in stirred tanks: Effect of drag models. *Chemical Engineering Journal*, 386:121554, 2020.
- [90] Francesca Scargiali, Alessandro D’Orazio, Franco Grisafi, and Alberto Brucato. Modelling and simulation of gas-liquid hydrodynamics in mechanically stirred tanks. *Chemical Engineering Research and Design*, 85(5):637–646, 2007.
- [91] Ramin Zadghaffari and Jafar Sadegh Moghaddas. Evaluation of drag force effect on hold-up in a gas-liquid stirred tank reactor. *Journal of chemical engineering of Japan*, 43(10):833–840, 2010.
- [92] Harvey D Mendelson. The prediction of bubble terminal velocities from wave theory. *AIChE Journal*, 13(2):250–253, 1967.
- [93] Shuli Shu and Ning Yang. Gpu-accelerated large eddy simulation of stirred tanks. *Chemical Engineering Science*, 181:132–145, 2018.
- [94] I Roghair, YM Lau, NG Deen, HM Slagter, MW Baltussen, M Van Sint Annaland, and JAM Kuipers. On the drag force of bubbles in bubble swarms at intermediate and high reynolds numbers. *Chemical engineering science*, 66(14):3204–3211, 2011.

- 
- [95] Xuedong Jiang, Ning Yang, and Bolun Yang. Computational fluid dynamics simulation of hydrodynamics in the riser of an external loop airlift reactor. *Particuology*, 27:95–101, 2016.
- [96] Akio Tomiyama, Isao Kataoka, Iztok Zun, and Tadashi Sakaguchi. Drag coefficients of single bubbles under normal and micro gravity conditions. *JSME International Journal Series B Fluids and Thermal Engineering*, 41(2):472–479, 1998.
- [97] Xiaosong Zhang, Jianhua Wang, and Decheng Wan. Euler–lagrange study of bubble drag reduction in turbulent channel flow and boundary layer flow. *Physics of Fluids*, 32(2):027101, 2020.
- [98] Giovanni Luzi and Christopher McHardy. Modeling and simulation of photobioreactors with computational fluid dynamics—a comprehensive review. *Energies*, 15(11):3966, 2022.
- [99] MMCG Warmoeskerken, J Feijen, and JM Smith. Hydrodynamics and power consumption in stirred gas-liquid dispersions. *Fluid Mixing*, 64:J1–J14, 1981.
- [100] Francesco Maluta, Alessandro Paglianti, and Giuseppina Montante. Prediction of gas cavities size and structure and their effect on the power consumption in a gas-liquid stirred tank by means of a two-fluid rans model. *Chemical Engineering Science*, 241:116677, 2021.
- [101] Ghanem F Oweis, IE Van der Hout, C Iyer, G Tryggvason, and Steven L Ceccio. Capture and inception of bubbles near line vortices. *Physics of Fluids*, 17(2):022105, 2005.
- [102] Huaiyu Cheng, Xinping Long, Bin Ji, Xiaoxing Peng, and Mohamed Farhat. A new euler-lagrangian cavitation model for tip-vortex cavitation with the effect of non-condensable gas. *International Journal of Multiphase Flow*, 134:103441, 2021.
- [103] Mamoru Ishii and Novak Zuber. Drag coefficient and relative velocity in bubbly, droplet or particulate flows. *AIChE journal*, 25(5):843–855, 1979.

## 8 Appendix A

Time averaged EDR measured at the output lines corresponding with the normalized EDR as depicted in Figure 20.

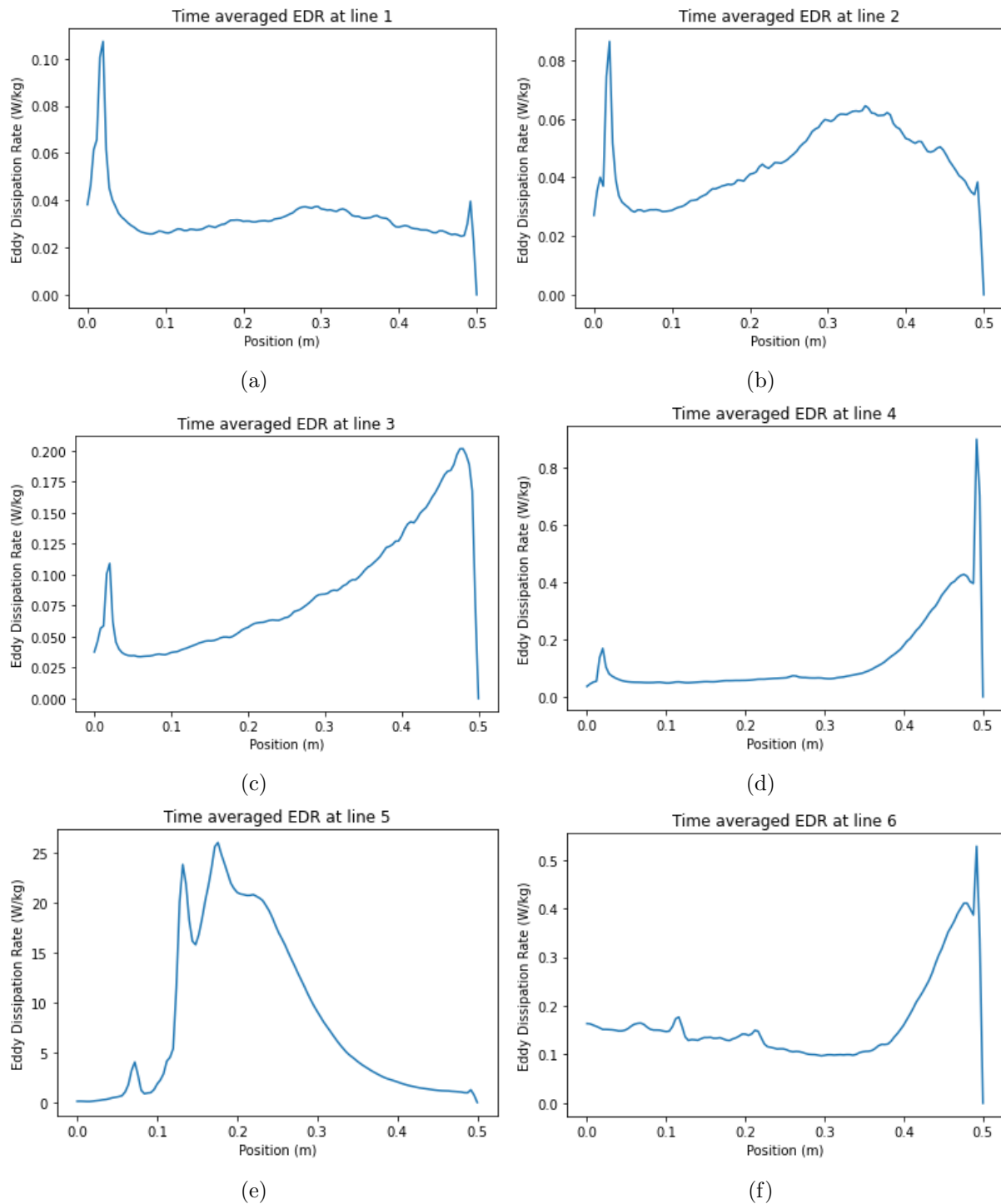


Figure 33: EDR per output line for the case with an agitation speed of 180 RPM and GFR of 0.00164 m<sup>3</sup>/s.

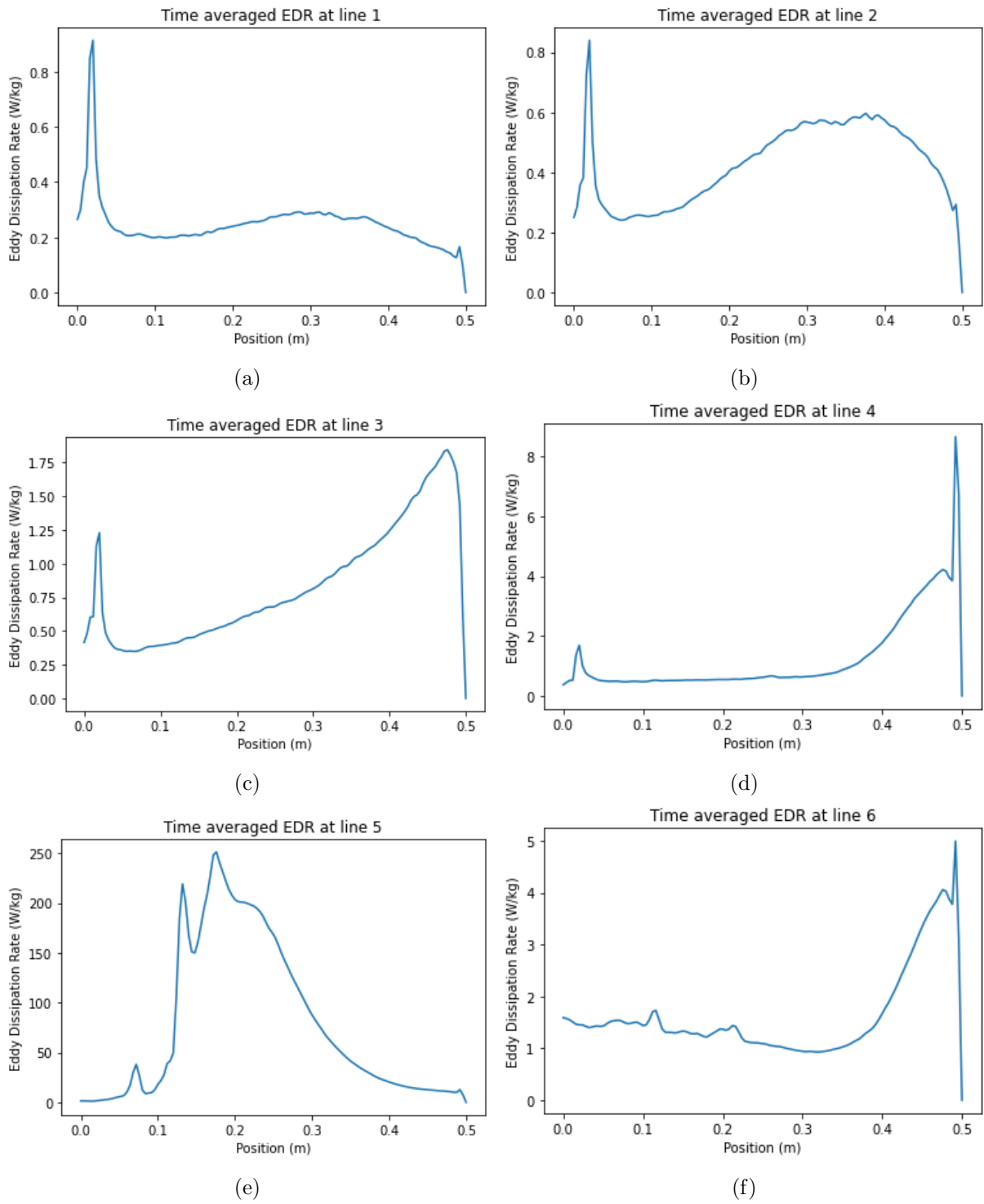


Figure 34: EDR per output line for the case with an agitation speed of 385 RPM and GFR of 0.00687 m<sup>3</sup>/s.

## 9 Appendix B

The selected parameters for the simulations. Note that settings such as: Injection Number Scale, Impeller size and RPM vary throughout the cases.

General	
Injection Option	VolumeFeed
Injection Geometry	ChildSurface
Volume Feed Rate Expr...	0
	Edit
Specified Feed Rate [#s]	0
Start Time [s]	10
Density [kg/m <sup>3</sup> ]	1.2
Size Distribution	
Distribution Type	Single
Diameter [m]	0.0015
Show Dist	Show
Fluid Interaction	
Gravity/Buoyancy Force	On
Virtual Mass	On
Pressure Gradient	Off
Lift Saffman	Off
Drag Force Model	FreeParticle
Two way coupling	ThirdLaw
Fluid-Particle Force	
	Edit
Static Body Interaction	
Tank Option	Bounce
Break-Up/Coalesce	
Breakup Enabled	On
Coalesce Enabled	On
Representation	Parcel
Breakup Model	UnifiedModel
Start Time [s]	10
Surface Tension [N/m]	0.072

(a)

Mass Transfer Coeffici...	
Mass Transfer Coeff	Off
Advanced	
Injection Number Scale	20000
Modeled Particles [#s]	0
Max Coalesce Diamete...	Custom
Max Coalesce Diamete...	0.005
Initial Velocity Type	NONE
Compute Particle Dist	On
Deletion Diameter [m]	1e-05
Third Law Num Scaling...	0.5
Injection Ramp Time [s]	0
Bubble Pressure	Off
Reference Pressure [Pa]	101325
Reference Temperature...	273.15

(b)

Figure 35: Bubble Settings

**General**

Location [m]

X	0
Y	0
Z	0

Axis

-0
1
0

Motion Type

Rotation

Rotation Speed [rpm]

133.2

Motion Option

Disabled

**Advanced**

Ramp Time Mode

Auto

Ref Thickness [m]

0.139333

Ref Diameter [m]

0.696667

Calc Internal Mass

Off

**Display Axis Attributes**

Visible

Shown

Mode

Wire

Color

Width

(a) Moving Wall Settings

**General**

Boundary Type

Interpolated

Wall Function

Off

Wall Velocity

Off

Compute Contact Line Force

On

Contact Angle [deg]

71

Mount Point [m]

X	0
Y	0
Z	0

Fluid Interaction

On

(b) Static Wall Settings

Figure 36: Wall Settings

**General**

Rheology Type

Newtonian

Density [kg/m<sup>3</sup>]

1000

Newtonian Nu [m<sup>2</sup>/s]

1e-06

Turbulence Model Type

LES

Smagorinsky Coefficient

0.1

Custom Accel Enabled

Off

Pressure [Pa]

101325

Enable Surface Tension

On

Surface Tension [N/m]

0.072

Enable Vof Ibm Normal Force

Off

Bubble Volume Coupling

On

Bubble Free Surface Interact...

Remove

Bubble Removal Condition

AllBubbles

Bubble Removal Volume Fr...

0.1

Enforce Conservation

On

**Fluid-Particle Convert**

Option

Off

**Initial Conditions**

Initial Condition Default

Empty

Fluid Height Box Condition

Fluid

Figure 37: Free Surface Settings

## 10 Appendix C

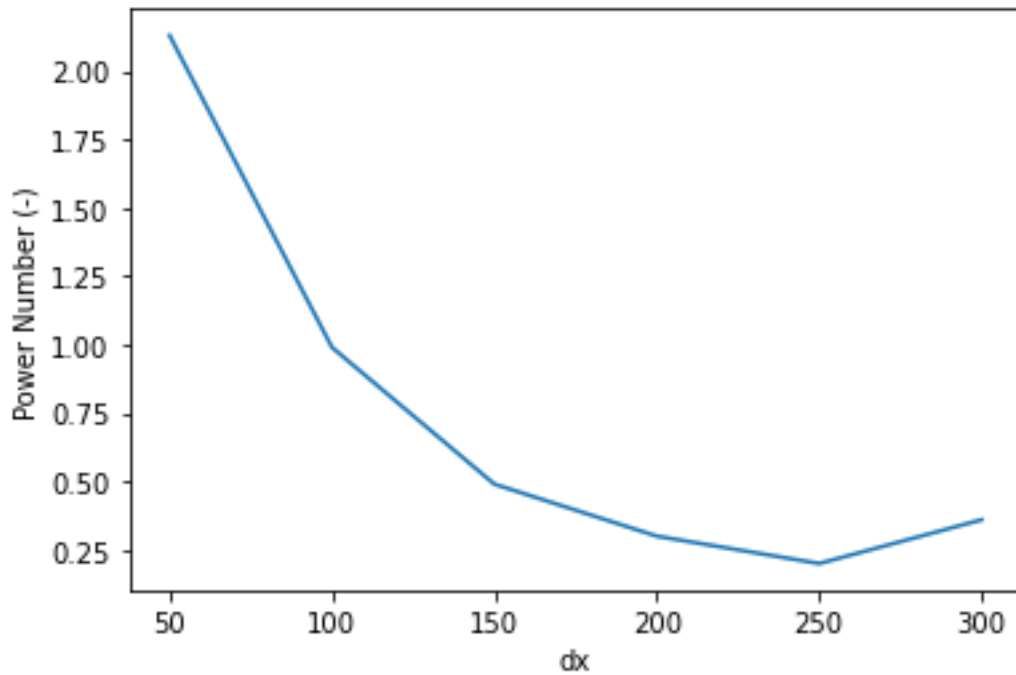


Figure 38: Grid convergence for the verification case. As dx is increased, the Power number converges.

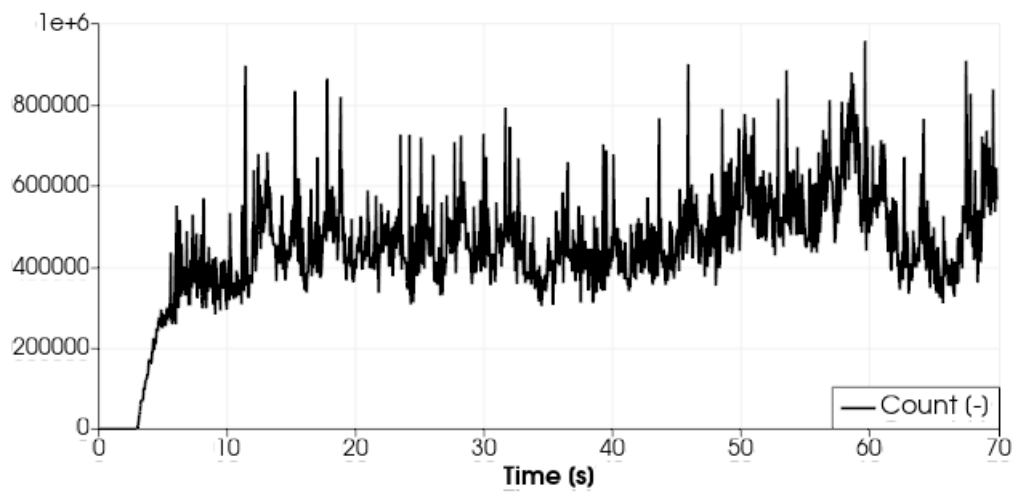


Figure 39: By extending the run time of the simulations, it is observed that the amount of bubbles present in the system is reduced before it is increased.